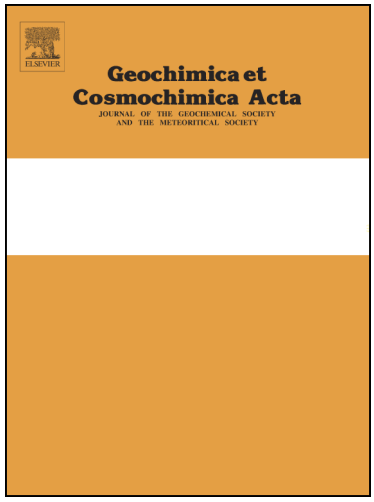

Ahrensite, γ-Fe_2SiO_4, a new shock-metamorphic mineral from the Tissint meteorite: implications for the Tissint shock event on Mars

Chi Ma, Oliver Tschauner, John R. Beckett, Yang Liu, George R. Rossman, Stanislav V. Sinogeikin, Jesse S. Smith, Lawrence A. Taylor

PII: S0016-7037(16)30211-3
DOI: http://dx.doi.org/10.1016/j.gca.2016.04.042
Reference: GCA 9737

To appear in: *Geochimica et Cosmochimica Acta*

Received Date: 11 July 2014
Accepted Date: 21 April 2016

Please cite this article as: Ma, C., Tschauner, O., Beckett, J.R., Liu, Y., Rossman, G.R., Sinogeikin, S.V., Smith, J.S., Taylor, L.A., Ahrensite, γ-Fe_2SiO_4, a new shock-metamorphic mineral from the Tissint meteorite: implications for the Tissint shock event on Mars, *Geochimica et Cosmochimica Acta* (2016), doi: http://dx.doi.org/10.1016/j.gca.2016.04.042

Revision 2 - 03/30/2016

Ahrensite, γ-Fe_2SiO_4, a new shock-metamorphic mineral from the Tissint meteorite: implications for the Tissint shock event on Mars

Chi Ma[a,*], Oliver Tschauner[b], John R. Beckett[a], Yang Liu[c], George R. Rossman[a], Stanislav V. Sinogeikin[d], Jesse S. Smith[d], Lawrence A. Taylor[e]

[a]*Division of Geological and Planetary Sciences, California Institute of Technology, Pasadena, California 91125, USA*

[b]*High Pressure Science and Engineering Center and Department of Geoscience, University of Nevada, Las Vegas, Nevada 89154, USA*

[c]*Jet Propulsion Laboratory, California Institute of Technology, Pasadena, California 91109, USA*

[d]*HPCAT, Geophysical Laboratory, Carnegie Institution of Washington, Argonne, Illinois 60439, USA*

[e]*Planetary Geosciences Institute, Department of Earth and Planetary Science, University of Tennessee, Knoxville, Tennessee 37996, USA*

* Corresponding author. Tel.: +1 626 395 6253

E-mail address: chi@gps.caltech.edu

Abstract

Ahrensite (IMA 2013-028), γ-Fe_2SiO_4, is the natural Fe-analog of the silicate-spinel ringwoodite (γ-Mg_2SiO_4). It occurs in the Tissint Martian meteorite, where it forms through the transformation of the fayalite-rich rims of olivine megacrysts or Fe-rich microphenocrysts in contact with shock melt pockets. We report the first comprehensive set of crystallographic, spectroscopic, and quantitative chemical analysis of type ahrensite, and show that concentrations of ferric iron and inversion in the type material of this newly approved mineral are negligible. We also report the occurrence of nanocrystalline ringwoodite in strained olivine and establish correlations between grain size and distance from melt pockets. The ahrensite and ringwoodite crystals show no preferred orientation, consistent with random

nucleation and incoherent growth within a highly strained matrix of olivine. Grain sizes of ahrensite immediately adjacent to melt pockets are consistent with growth during a shock of moderate duration (1-10 ms).

Keywords: Ahrensite, γ-Fe_2SiO_4, new high-pressure mineral, shock metamorphism, nanomineral, ringwoodite group, Tissint meteorite, Martian shergottite, synchrotron diffraction.

1. INTRODUCTION

Bolide impacts represent a fundamental process in the construction and destruction of planetary bodies, especially early in the history of the solar system (e.g., Neukum et al., 2001; Canup, 2012; Morbidelli et al., 2012; Fassett and Minton, 2013; Marchi et al., 2013). On the Earth, active surficial processes tend to bury, modify, or destroy the features produced by these events over geologic time; but on Mars, the Moon, asteroids, and airless bodies in general, the scars of past impact events are clearly visible even with a casual perusal of the surficial geology. All Martian meteorites, previously launched from the surface of Mars, exhibit evidence for significant shock effects; shergottites and chassignites have been especially heavily shocked and contain a broad range of high-pressure phases (e.g., Fritz and Greshake, 2009; Baziotis et al., 2013; El Goresy et al., 2013b; Walton et al., 2014). Thus, any interpretation of earlier conditions, resulting from processes on Mars that can be drawn from SNC meteorites, must take into account possible modifications through the launching-shock event. Shock metamorphism affects the texture, chemistry, and mineralogy of Martian meteorites and, potentially, the record of radionuclide systems (Bouvier et al., 2008; El Goresy et al., 2013a; Humayun et al., 2013), although the influence of shock on the discordia of radioisotope systems is under active debate (e.g., Bloch and Ganguly, 2014). The deep gravity well of Mars also makes Martian meteorites better analogs for large terrestrial impacts than are the heavily shocked ordinary chondrites.

The Tissint meteorite is an olivine-phyric shergottite, consisting mainly of pyroxene (mostly pigeonite and subcalcic augite), olivine (magnesian megacrysts with thin ferroan rims and microphenocrysts), maskelynite (shock-produced, plagioclase-composition glass), and accessory chromite, ilmenite, merrillite, and FeS, plus scattered shock-melt pockets and rare melt veins with associated high-pressure phases. Walton, et al. (2014) described residual grains of the original igneous minerals within melt veins and/or pockets from Tissint that survived the shock

event; these have not been observed in the melt pockets examined in this study. Here, we characterize grain dimensions of ringwoodite and the recently established high-pressure mineral, ahrensite (Fe_2SiO_4 spinel) as a function of distance from melt pockets; these provide an independent constraint on the duration of the Tissint shock event.

The olivine structure is closely related to the spinel structure. Upon compression, forsterite and its Co-, Fe-, and Ni-isomorphs transform to the cubic $Fd\bar{3}m$ spinel structure (e.g., Ringwood, 1958, 1962; 1963; Ringwood and Major, 1966); but among these, only two, ringwoodite and ahrensite, are currently known to exist in nature. In this work, we give the first comprehensive chemical, spectroscopic and crystallographic account of the new mineral ahrensite [γ-$(Fe,Mg)_2SiO_4$, IMA-2013-028]. Ahrensite is the Fe end-member of the γ-Mg_2SiO_4-Fe_2SiO_4 series of silicate-spinels, which are critical constituents in the mantles of Earth, Mars, and Venus (e.g., Bertka and Fei, 1997; Stixrude and Lithgow-Bertelloni, 2011; Armann and Tackley, 2012). Since ringwoodite was the first known silicate mineral with the spinel structure, the convention (Mills et al., 2009) is to use ringwoodite as the group name. Thus, ahrensite is the second member of the ringwoodite group of minerals. Ahrensite refers to a γ-$(Fe,Mg)_2SiO_4$ solid solution with Mg# [100Mg/(Mg + Fe) computed on a molar basis] < 50 and ringwoodite to those with Mg# > 50.

Ringwoodite is commonly observed in highly shocked meteorites from the Moon, Mars, and H and L ordinary chondrites (e.g., Binns et al., 1969; Kimura et al., 2003; Xie and Sharp, 2007; Zhang et al., 2011; Baziotis et al., 2013; Walton et al., 2014). In some L5-L6 ordinary chondrites, Mg#s are low enough so that the phase being described is actually an ahrensite [i.e., Mg# < 50; Xie et al., 2002; Feng et al., 2011], with the mole % of Fe_2SiO_4 as high as 98% in the L6 chondrite Umbarger (Xie et al., 2002). However, these descriptions did not lead to approval of a new mineral by the Commission on New Minerals, Nomenclature, and Classification (CNMNC). In this report, we provide full sets of chemical and structural information that establish ahrensite, γ-$(Fe,Mg)_2SiO_4$, as a new mineral based on occurrences in the Martian meteorite Tissint and use this phase to constrain shock processes. Ma et al. (2014a,b) give preliminary reports of the results described in this work.

The CNMNC of the International Mineralogical Association has approved "ahrensite" (IMA 2013-028) (Ma et al., 2013). The name was given to honor Caltech geophysicist Thomas J. Ahrens (1936-2010) for his pioneering and fundamental contributions to high-pressure mineral

physics and planetary sciences, many of which involved the use and interpretation of shock effects in natural rocks and synthetic materials.

2. SAMPLES AND METHODS

2.1. Sample information for type material and other occurrences

The Tissint meteorite is a recent meteorite fall associated with an observed fireball event near Tissint and Tata, Morocco, on July 18, 2011. Based on mineral chemistry (molar Fe/Mn in olivine and pyroxenes), noble-gas signatures, and bulk trace-element and oxygen-isotope compositions, this meteorite has been classified as Martian (Aoudjhane et al., 2012; Irving et al., 2012; Murty et al., 2012). Tissint is the fifth fall of a Martian meteorite and the first since Zagami in 1962. It is a depleted olivine-phyric shergottite with abundant shock features and has been the subject of intensive study since its fall, largely because it is so fresh (e.g., Steele et al., 2012; Baziotis et al., 2013; Walton et al., 2014 and references therein).

We discovered ahrensite in three polished thin sections of Tissint prepared from one ~10 g fragment with a partial fusion crust. Type material in Tissint sections UT1, UT2 and UT3 (e.g., Figs. 1-2, S1; formerly referred to as MT-1, 2, 3 by Baziotis et al., 2013) has been deposited in the Meteorite Collection of the Frank H. McClung Museum at the University of Tennessee, Knoxville, Tennessee 37996, USA. Polished thin sections of the olivine-phyric shergottites DaG 476, NWA 6710, NWA 4925, and SaU 005 were also examined for ahrensite and ringwoodite, in areas between melt pockets and olivine, the petrographic setting in which ahrensite occurs in Tissint. Phases in these regions were, however, composed of terrestrial alteration products, and shock-induced high-pressure polymorphs of olivine, if present in the original meteorite sampled by the analyzed sections, have been lost due to weathering.

2.2. Analytical methods

For ahrensite in Tissint, electron probe microanalysis (EPMA), high-resolution scanning electron microscope (SEM), electron back-scatter diffraction (EBSD), synchrotron X-ray diffraction, microRaman spectroscopy, and optical microscopy were used to determine its composition, physical properties, and structure, and to characterize associated phases.

Back-scatter electron (BSE) imaging and EBSD were carried out using a ZEISS 1550VP field-emission SEM. Chemical analyses of type ahrensite and associated minerals were obtained,

using a JEOL 8200 electron microprobe (WDS: 15 kV; 20 nA; beam in focused mode) interfaced with the Probe for EPMA program from Probe Software, Inc. Standards for these analyses were synthetic fayalite (Si*K*α, Fe*K*α), Shankland forsterite (Mg*K*α), synthetic Mn_2SiO_4 (Mn*K*α), synthetic anorthite (Al*K*α, Ca*K*α), Amelia albite (Na*K*α), Asbestos microcline (K*K*α), synthetic TiO_2 (Ti*K*α), and synthetic Cr_2O_3 (Cr*K*α). Quantitative elemental microanalyses were processed with the CITZAF correction procedure (Armstrong, 1995) and representative analytical results are given in Table 1.

Synchrotron diffraction data were collected at the undulator beamline 16-IDB (APS, Argonne National Laboratory) using a primary beam energy of 20.072 keV (0.6177Å) and about 94% horizontal polarization, monochromatized by a double-crystal Si (111) monochromator. The sample consisted of a doubly polished thin section of Tissint mounted on a glass slide. A Pilatus 1M hybrid-pixel array detector was used for collecting the sample diffraction data. The X-ray beam was initially focused to a rectangular ~ 4×5 μm^2 area on the top surface of the thin-section, where the Tissint sample was exposed, by vertical and horizontal Kirkpatrick-Baez mirrors of 200 mm focal length. Since the beam passed through both the meteorite and the underlying glass slide upon which the sample was mounted, diffraction pattern images were first corrected for diffuse scattering from the glass slide using the Fit2D background image subtraction module (Hammersley et al., 1996), and then integrated and corrected for geometric distortion from detector tilt using Fit2D (Hammersley et al., 1996). Ahrensite in thin-section UT2 was scanned in 5 μm steps horizontally and vertically through the focused X-ray beam, and diffraction patterns were recorded in transmission geometry at each step. Rietveld refinement of the ahrensite structure was conducted with the program PowderCell (Kraus and Nolze, 1996), as detailed below.

The optical spectrum of ahrensite was collected in the 380-1080 nm region, with the silicon diode-array microspectrometer described in Rossman and Taran (2001), and in the near-infrared region with a Thermo-Nicolet iS50 FTIR fitted with a Continuμm infrared microscope using a MCT-A detector and a silica beamsplitter interrogating a 25 × 25 μm area. The area used for the spectrum was centered on the UT1 sample shown in Fig. 3, in the bluish-green area labeled “ahrensite”.

Raman spectroscopic microanalysis was carried, out using a 514.3 nm solid-state laser in a Renishaw M1000 micro-Raman spectrometer system, on type ahrensite in section UT2 and on

green ringwoodite in section UT1, using the methods described in Ma and Rossman (2008, 2009). The spot size was about 2 μm.

3. RESULTS

3.1. Petrographic characterization

Figures 1 and S1 provide an overview of the Tissint rock in UT2, which contains the type material. Ahrensite was identified near shock-melt pockets, where they contact Fe-rich rims of olivine megacrysts, including the olivine megacryst shown in Fig. 1, which is zoned from $Fo_{64}Fa_{36}$ in the core to as ferroan as $Fo_{40}Fa_{60}$ in the rim. A melt pocket occurs within the Fe-rich rim region of the megacryst and it is around the margins of this melt inclusion that the type ahrensite occurs (Fig. 2a). The ahrensite is polycrystalline (Fig. 2b). A thin layer of bridgmanite, $(Mg,Fe)SiO_3$ in the perovskite structure (Tschauner et al., 2014), plus wüstite occurs between ahrensite and the melt pocket (Fig. 2c). This phase assemblage and its origin will be described in a separate publication.

In Tissint sections UT1 - UT3, ahrensite and ringwoodite form polycrystalline aggregates, 5 - 20 μm across in the plane of the thin sections, composed of irregular to subhedral crystals 2 (see below) - 500 nm in diameter. Crystal size of the ahrensite-ringwoodite phase decreases with increasing distance from a melt pocket, as illustrated in Figs. 2b and 2c. The aggregates are bluish green in color and translucent (Fig. 3). The density as calculated from the empirical formula and the crystal structure, as described below, is 4.26 g/cm^3.

High-pressure minerals identified by chemical composition plus EBSD and/or synchrotron diffraction in the Tissint sections considered in this study are ahrensite, ringwoodite, bridgmanite (Tschauner et al., 2014), wüstite-periclase, wadsleyite, tissintite (a newly-approved $(Ca,Na,\square)AlSi_2O_6$ clinopyroxene; Ma et al. 2015), xieite (a high-pressure polymorph of chromite), tuite, and stishovite. Baziotis et al. (2013) also reported the high-pressure minerals akimotoite, majorite, and lingunite in the same sections we studied but these identifications were based on the interpretation of Raman spectra without additional structural confirmation. Additional high-pressure phases, including diamond and jadeite, have been reported in other samples of Tissint based on Raman and TEM analysis (El Goresy et al., 2013b; Walton et al., 2014).

Ahrensite in Tissint is invariably associated with olivine that was in contact with a melt pocket. We did not observe ahrensite adjacent to shock melt veins in thin sections UT1-3, although it has been reported in other sections (Walton et al. 2014). We note that ahrensite-ringwoodite crystals UT1-3 show no preferred orientation as evidenced by EBSD mapping, even though they grow within a single crystal matrix of olivine. This implies that nucleation and growth were not controlled by a single set of crystallographic sites or interfaces. It is also important to note in BSE images that crystal-size increases systematically with decreasing distance from a melt pocket (e.g., Figs. 2b and 2c). The grain size of ahrensite-ringwoodite and its variation with distance is an important indicator of shock intensity and thermal history.

In sections UT1 - UT3, melt pockets come in two major textural forms. The first, as shown in Figs. 1-2, is relatively small (40 – 120 μm in size), consisting mostly of a vitreous kernel whose bulk composition is consistent with a mixture of adjacent major matrix phases [Fe-rich rim olivine (32% by weight), augite (36%), pigeonite (21%), and plagioclase (11%) for the melt pocket shown in Fig. 2a; see also Fig. 4a]. A second, more common, texture of melt pockets is shown in Fig. 5. These are large (200 – 900 μm in size in UT1-3 and even larger in other Tissint sections) irregular bodies. They are mainly composed of an intimate mixture of pigeonite and fayalite, but also include amorphous regions and inclusions of tissintite, wüstite, troilite, xieite, chromite, ilmenite, and merrillite, which were confirmed by EBSD. Maskelynite, pyroxene, ilmenite, and bridgmanite plus wüstite are observed as contacting phases with the melt pocket for the example shown in Figs. 5 and S3. In each of six interfaces between the melt pocket and olivine megacryst we examined in detail in UT1-3, there is an intervening layer of bridgmanite (Tschauner et al., 2014) plus wüstite and of stishovite plus wüstite that separates the melt pocket from ringwoodite and/or ahrensite.

Petrographic differences between the large and small melt pockets are likely due to differences in pressure during quenching. Large pockets quenched at pressures low enough for fayalite and pigeonite to crystallize. Some of the small pockets quenched at pressures high enough to allow the retention of trace amounts of high-pressure phases, like the fine-grained stishovite, revealed by synchrotron diffraction in this study.

3.2. Chemical composition of ahrensite

The general formula of ahrensite is $(Fe,Mg)_2SiO_4$ with an end-member formula of Fe_2SiO_4. The type ahrensite has an empirical formula (based on 4 O atoms *pfu*) of $(Fe_{1.06}Mg_{0.91}Mn_{0.02})Si_{1.01}O_4$ from EPMA (Table 1), whereas synchrotron X-ray diffraction suggests a formula of $(Fe_{1.12}Mg_{0.86}Si_{0.02})(Si_{0.98}Fe_{0.02})O_4$. The difference in composition between the two approaches is real and reflects different sampling volumes. An EPMA analysis samples a small near-surface volume of ~ 1 μm^3.The synchrotron diffraction analysis was conducted in transmission mode with the beam passing completely through the thin section, thereby sampling a volume given by the ~ 4 × 5 μm area of the X-ray beam but extending throughout the entire ~ 30 μm thick section. In Tissint, observed compositions for silicate spinels ranged from $(Fe_{1.06}Mg_{0.91}Mn_{0.02})Si_{1.01}O_4$, an ahrensite, to $(Mg_{1.11}Fe_{0.85}Mn_{0.02})Si_{1.01}O_4$, a ringwoodite with Mg# increasing with distance from melt pockets (e.g., Fig. 4b).

3.3. Crystallography and grain size

X-ray diffraction patterns of ahrensite exhibit smooth Debye fringes without radial modulation of their intensities from texture or superimposed reflections from coarser crystallites (Fig. 6). This result is consistent with mapping by EBSD, which shows no texture or the presence of grains larger than 300 nm in diameter, except within ~5 μm closest to the melt pocket. Rietveld refinement of the synchrotron data via PowderCell yielded final profile parameters: U = 0.421, V = 0.187, W = 0.002, mixing parameters n_a = 1.000, n_b = 0.018, for a pseudo-Voigt profile function, and a scale factor of 2.581. The refinement converged to a profile-weighted refinement factor R_{wp} of 0.038 (with an unweighted refinement factor R_p of 0.013). As a crosscheck for model validity, we made a LeBail extraction (R_p = 0.02) and conducted a reversed Monte Carlo optimization (Putz et al., 1999) based on the extracted structure factors, |F(*hkl*)|, which converged to a R_F of 0.048. The refinement confirmed that type ahrensite is cubic with space group $Fd\bar{3}m$, a = 8.1629(2) Å, V = 543.92(7) $Å^3$, Z = 8, and is isotypic with ringwoodite (see below). EBSD patterns of ahrensite in Tissint (Fig. 7) match well to this structure, with mean angular deviations (MAD) as low as 0.38º. Atomic coordinates, site occupancies, and isotropic displacement parameters (B_{iso}) are given in Table 2. The extracted |F(*hkl*)| and X-ray powder diffraction data (observed *hkl*, d-spacings, and relative intensities) are listed in Table 3, for the used X-ray wavelength of 0.6177 Å; the powder diffraction pattern is

shown in Fig. 8 for a region approximately 5 μm away from the melt pocket. Moving away from the type ahrensite material towards the interior of the megacryst, the cell parameter of the spinel gradually decreases toward that of ringwoodite.

Marked broadening of synchrotron diffraction peak profiles further away from the melt pockets (Figs. 8 and 9) indicates a decrease in the crystal grain size. We quantified this effect using PowderCell (Kraus and Nolze, 1996) to model the observed diffraction patterns and applied the Scherer equation to the full width at half maxima of up to 36 reflections to compute the average grain sizes (e.g., Akram and Anis-ur-Rehman, 2013). Results are shown for the type region (Fig. 2) in Figs. 6 and 9 (for the diffraction images given in Figs. 8c-e). Although ahrensite was identified in the diffraction image of 8b, even the (311) peak was, in this case, too weak to reliably support modeling of the profile. Between 5 and 30 μm from the melt pocket, the average grain size of ahrensite-ringwoodite decreases by more than an order of magnitude, from 39 - 45 nm to 2 - 3 nm. Ahrensite-ringwoodite within ~5 - 15 μm of the melt pocket is sufficiently coarse-grained (>~50 nm) that it can be imaged using BSE and we used this technique to show that grain size increases from ~50 nm at 5 μm distance from the melt pocket to ~450 nm at ~1 μm (i.e., at the interface with the bridgmanite-wüstite phase assemblage, which is ~1 μm thick in the region used for the measurements (e.g., Fig. 2c). These results are compiled in Fig. 10. For the type example in UT2, synchrotron- and BSE-derived grain sizes yield subparallel lines that are offset by ~15 μm, a consequence of the geometry of the interface between the melt pool and "wall-rock" below the plane of the section and the difference in how grain size is measured using BSE and synchrotron. BSE provides the grain size in the plane of the section whereas a synchrotron beam samples the entire column through the thin section. We show in the Supplement (Fig. S4) that the configuration for the type example is consistent with a melt-"wall-rock" interface that extends out under the melt pool as seen in the plane of the thin section at an angle of ~45° and that distances as measured in the plane of the thin section by BSE are, therefore, ~30% longer than corresponding perpendiculars to the melt-"wall-rock" interface in 3-D. The UT1 example is more complex, as perhaps befits a microphenocryst (40 × 60 μm) in contact with an elongate (50 × 330 μm) melt pocket. Here, the grain-size data suggest a melt-"wall-rock" interface that undercuts the "wall-rock," as seen in the plane of the thin section, and is nonplanar. Nevertheless, the fact that near-interface grain sizes based on the BSE-data are

similar for both examples (i.e., ~400-500 nm) suggests that both examples experienced similar thermal histories. Overall, it is clear from Fig. 10 that there is a general decrease in grain size with distance from the melt pool and that this is qualitatively consistent with decreasing intensity of heating with increasing distance.

3.4. Spectroscopy

The Raman spectrum of the type ahrensite (sample UT2) is shown in Fig. 11, along with a spectrum from the intermediate region between ahrensite and olivine and the spectrum of adjacent olivine. Although the ahrensite spectrum has significant noise, several features can be identified. They are located at (in cm^{-1} Raman shift): 212 (broad), 294 (sharper), 576, 672, 795, 843 (the most intense), and 916 (broad). The same features are also seen in the spectrum of ahrensite with a composition of $(Fe_{1.01}Mg_{0.95}Mn_{0.02})Si_{1.01}O_4$ obtained in a pale portion of the grain used for the optical spectrum in sample UT1. The region between the ahrensite and olivine is devoid of any significant Raman features (Fig. 11), consistent with the spectrum of a highly disturbed material and in keeping with the observation that these regions also display no EBSD pattern.

Ahrensite is bluish-green in transmitted light (Fig. 3) with an optical spectrum (Fig. 12) dominated by a broad absorption band centered at approximately 870 nm. The corresponding optical spectrum of ringwoodite, taken from Keppler and Smyth (2005), is also shown in Fig. 9. It has a major band at ~815 nm and a second component at ~1150 nm. Keppler and Smyth (2005) assigned these features to spin-allowed absorptions arising from octahedrally coordinated Fe^{2+}. There is an additional absorption feature in their spectrum at ~570 nm. They assign this feature, which absorbs in the green portion of the spectrum, to inter-valence charge transfer between Fe^{2+} and Fe^{3+}. This is the primary reason that synthetic Fe-bearing ringwoodites, including that of Keppler and Smyth (2005), are blue. This feature is not prominent in the ahrensite spectrum, which means that ahrensite transmits light with more green components and indicates that there is little Fe^{3+} in the Tissint ahrensite, consistent with ahrensite chemistry based on EPMA analysis, which requires no Fe^{3+}, within error, to produce an X_2SiO_4 stoichiometry.

The ahrensite optical spectrum lacks any obvious spectroscopic resolution of the two expected Fe^{2+} spin-allowed absorptions. The most likely reason for this is that the optical beam, unlike the EBSD and Raman results that are primarily surface analyses, intercepts regions of

different materials (ahrensite and ringwoodite solid solutions), as well as possible cracks in the probed material. These contaminants would serve to contribute broad, poorly defined components to the spectrum and lead to broadening. The ahrensite spectrum, nevertheless, indicates that octahedral Fe^{2+} is the principal optically active ion. It is worth further noting that the spectrum of Fe^{2+} in a tetrahedral site in spinels is well known to have absorption bands in the 2000 nm region (e.g., Taran and Rossman, 2001) that are about an order of magnitude stronger than those of octahedral Fe^{2+} in olivine. The optical spectrum of ahrensite shows no hint of such features and, therefore, provides no indication for tetrahedral Fe^{2+}. This is consistent with the structure refinement based on the X-ray diffraction data (Table 2), which constrains the amount of Fe on the tetrahedral site to between 0 and 3 %.

4. DISCUSSION

During the passage of a shock wave through the Tissint parent body rock, temperature differences were generated between adjacent grains of olivine, pyroxene, and feldspar grains due to the different shock impedances of these minerals. However, these differences cannot account for the high local temperatures of shock-generated melt pockets, for which plausible mechanisms include: 1) collapse of voids upon passage of the shock wave front (e.g., Sharp and DeCarli, 2006; Tschauner et al., 2009); 2) local transient peaks of dynamic stress generated by the interference of non-planar shock waves (Stöffler et al., 1986; Fritz and Greshake, 2009). Void collapse results in heating through rarefaction at the front-side of a void (relative to the shock front) while, at the same time, this hot material is accelerated toward and eventually impacts onto the rear-side of the void. The surrounding material is at a lower temperature, but initially higher shock pressure. During shock, stress patterns evolve on the scale of the particle velocity (km/s), whereas temperature gradients decrease by radiative and conductive heat transfer. The latter is comparatively much slower but, due to absorbance of incandescent light by the wall rock, radiative and conductive heat transfer is coupled. A number of authors have appealed to rapid thermal quench near melt-host-rock contacts to account for observed high-pressure phase assemblages in melt veins and pockets (e.g., Xie et al. 2006; Sharp and DeCarli 2006; Shaw and Walton 2013; Tschauner et al. 2014); these regimes of rapid temperature quench occur during shock release at pressures that depend on the total heat of the pocket and it is this process that

permits the conservation of bridgmanite and akimotoite in melt veins and at the border of melt pockets.

Reverberative pressure homogenization in solid polycrystalline aggregates has been shown to be inefficient in three dimensional aggregates: Luo et al. (2010) and Pham et al. (2011) showed in three-dimensional shock simulations on bicrystals that the stresses evolve over time in such aggregates and homogenize on time scales orders of magnitude longer than that of the ratio of grainsize over particle velocity. In addition, they showed that extensive transient local stress- and temperature-excursions occur. Local high dynamic stresses result in elevated temperatures when released to the background dynamic stress state. Thus, a sufficiently high stress excursion can also generate melt pockets that survive stress-equilibration due to the much slower thermal equilibration. In a melt, the shock pressure homogenizes on time scales correlated with the particle velocity because initial or transient stress differences induce turbulent mixing such as Richtmyer-Meshkov instabilities (Tschauner et al., 2005). High-pressure phase assemblages in shocked meteorites are restricted to the vicinity of hot spots (shock melt pockets and melt veins) because only in these regions were temperatures high enough to overcome kinetic barriers to nucleation and growth (e.g., Stöffler et al., 1991; Tomioka and Fujino, 1997; Xie and Sharp, 2007; Tschauner et al., 2014).

As noted above, Tissint is an olivine-phyric shergottite in which olivine megacrysts display a Mg-rich core, with Fe-enrichment towards the rim (e.g., Fig. 1a). These are igneous features predating shock. Ahrensite and ringwoodite repeat this chemical zoning pattern in their spatial distribution (Fig. 4b). Thus, they do not form as part of a heterogeneous reaction. Consequently, two-key conditions must be simultaneously satisfied if ahrensite is to form: 1) there must be an olivine of suitable composition (i.e., Mg# < 50) and 2) there must be an environment of sufficiently high pressure and temperature. These conditions are met during impact, which can readily generate shock waves greatly exceeding 5 km/s (the minimum velocity to eject rocks off Mars; Fritz et al., 2005). Ahrensites, described as natural γ-Fe_2SiO_4, have been previously reported from shock-melt pockets in ordinary chondrites (e.g., Xie et al., 2002; Feng et al., 2011) and ringwoodites have been described in a wide variety of ordinary chondrites, lunar rocks, and Martian meteorites (e.g., Binns, 1969; Zhang et al., 2011; Walton et al., 2014) but, in this Discussion, we focus on the formation and growth of ahrensite-ringwoodite in Tissint.

We observed no grains of ahrensite/ringwoodite in Tissint larger than ½ μm in diameter (e.g., Figs. 1-2, 5, 10) and no aggregates of oriented spinel domains larger than 1μm. Upon shock release, crystals of high-pressure polymorphs may disintegrate into submicron domains, but, in such cases, orientational relationships among the domains are preserved and this is not observed. The composition of ahrensite-ringwoodite solid solutions evolve with distance from the center of an olivine grain, similar to the way that fayalite-forsterite solid solutions do in its untransformed region (e.g., Fig. 4). Thus, no substantive Fe-Mg diffusion occurred in the ahrensite/ringwoodite region during or in the immediate aftermath of the shock. These compositional features are consistent with a transition of olivine to the spinel structure occurring in the solid state.

We noted above that the grain size of ringwoodite decreases with increasing distance from the adjacent melt pocket, reflecting the decrease of temperature with distance from the local heat source. More importantly, at distances of 30 - 80 μm from melt pockets, referenced to the top plane of the thin section, we observe nanocrystalline ringwoodite with grainsize down to 2-3 nm in highly strained olivine single crystals. The powder diffraction patterns of nanocrystalline ringwoodite observed by synchrotron (Fig. 8) are caused by a considerable number of grains (at least of the order of 10^4 nano-crystallites within the diffraction volume). Absence of intensity variations along the Debye fringes implies absence of preferred orientation (Fig. 8), so that the observed grain size distributions reflect the growth of ahrensite or ringwoodite in the solid state during a shock event through an incoherent growth mechanism. There is no orientational correlation between ringwoodite nanocrystals and host olivine. Nucleation kinetics is likely to have been homogeneous.

Occurrences of ahrensite-ringwoodite described in this work fundamentally differ from those of Walton et al. (2014), who described ringwoodite (Rw) lamellae in olivine (Ol) host crystals near a shock vein in Tissint with $[011]_{Ol} \parallel \langle 110 \rangle_{Rw}$ and $(100)_{Ol} \parallel \{111\}_{Rw}$. They postulated heterogeneous nucleation of ringwoodite on defects in the host olivine followed by coherent growth, which accounts for the observed preferred orientation of the lamellae; they suggested that a mechanism analogous to that observed in static experiments by Kerschhofer et al. (2000) was operative, although the different orientations of lamellae in the experiments and Tissint imply that the mechanisms are not exactly equivalent. Lamellar ringwoodite has also been described in a variety of ordinary chondrites (Ohtani et al., 2004; Miyahara et al., 2010; Greshake et al., 2013) with grain size related to shock duration. These occurrences differ

texturally from the ahrensite/ringwoodite that we observe near Tissint melt pockets, where there is no common crystallographic relationship between the ringwoodite/ahrensite grains and the host olivine. At least in Tissint, in the vicinity of melt pockets there are mechanisms for the olivine → ringwoodite/ahrensite transformation that are different from the coherent lamellar growth mechanism reported by Kerschhofer et al (2000).

Some first order implications for Tissint are obtained independent of any details on the topography and cooling history of different shock-melt pockets. For example, previous estimates of peak shock pressures in Tissint, which range from 23 to 30 GPa (Baziotis et al., 2013; Walton et al., 2014), are consistent with the observation of bridgmanite-periclase aggregates lining the border of shock melt pockets (Fig 2). Adjacent to these aggregates, stishovite and wüstite form from the decomposition of ahrensite; with increasing distance, ahrensite is observed, and, finally, ringwoodite, with grain size of ahrensite/ringwoodite decreasing from micro- to nanocrystalline with increasing distance from the melt pocket (Figs. 8-10). Ringwoodite and ahrensite persisted metastably at pressures beyond their stability field because their free energy at those high pressure conditions were lower than those of olivine and fayalite (Walton et al., 2014). They didn't break down to the stable phase assemblage of wüstite plus stishovite or bridgmanite plus periclase during this time because the temperatures were too low and time too short for nucleation and growth of these phases. The lack of preferred orientation among the crystals suggests that the growth of ahrensite and ringwoodite from the highly strained olivine of Tissint does not obey the known static growth mechanisms of Kerschhofer et al. (2000) or Mosenfelder et al. (2001) and, therefore, the experimentally determined growth rates are not necessarily applicable.

A key constraint on shock conditions lies in the evolution of grain size with increasing distance from the melt pocket (Fig. 10). In the caption to Fig. S4, we show that the surface of the original olivine macrocryst in the type sample extends out under the melt pool at a ~45° angle to the plane of the section; thus, ahrensite and ringwoodite grains in BSE images are ~30% closer to the melt pocket than they appear to be in the plane of section. Correcting for this effect and extrapolating the BSE-derived grain sizes as a function of distance to 2.5 nm, the smallest grains detected by XRD, we obtain a distance of ~23 µm from the melt pocket. A shock metamorphism model for the type location of ahrensite in Tissint must, therefore, account for

~0.5 μm diameter crystals within 1 μm of the melt pocket and ~2.5 nm diameter crystals at ~23 μm.

To illustrate how grain-size distributions might be inverted to constrain shock conditions, we used grain growth kinetics in Kerschoffer et al. (2000) and calculated total growth (i.e., half the grain diameter) for ringwoodite growing in a matrix of forsterite as a function of inverse temperature for specified shock durations (Fig. 13). The temperatures shown in Fig. 13 do not take thermal history into account; they should be viewed as effective temperatures for the transformation (i.e., these will be lower than peak conditions during growth and higher than the closure temperatures). Incubation periods for nucleation, interference from adjacent grain boundaries, and the effect of Fe/Mg>0 are also ignored. Available data for Fe-bearing magnesian olivines (Mosenfelder et al., 2001) suggest that growth rates are a weak function of Fe content but ahrensites and Fe-rich ringwoodites have yet to be tested. Delayed nucleation extends the required time period for grain growth and would, in the context of our example, translate into higher effective temperatures for a given shock period. We also note that experiments underlying the plotted lines were performed for a shock pressure of 18 GPa. Although the activation volume is zero within error for the forsterite - ringwoodite transformation (Mosenfelder et al., 2001), one might reasonably expect faster grain growth for higher pressures at constant temperature because of greater departures from equilibrium.

Consider first the solid lines in Fig. 13; these refer to incoherent growth via experiments of Liu et al. (1998), as given by Kerschhofer et al. (2000). Similar results are obtained using models of Mosenfelder et al. (2001), assuming the activation volume for growth to be zero. From Fig. 13, the effective temperature for the growth of a 0.5 μm diameter grain is 2104K for a shock duration of 1 ms and 1616K for a 2.5 nm grain. These temperatures decline with increasing shock duration (e.g., 1510K and 1242K, respectively, for a 1000 ms shock) as does the difference between them (~487° for a 1 ms shock to ~268° for a 1000 ms shock). Since the 0.5 and 2.5 nm are ~1 and ~23 μm from the melt pocket (in 3-D), a temperature gradient into the megacryst of 10-20°/μm during grain growth and temperatures at 20-25 μm well above the principal Hugoniot (430K at 28 GPa; Raikes and Ahrens, 1979) are implied. From Fig. 13, there is a direct trade-off between shock duration and effective temperature, with longer shocks requiring lower temperatures for the growth of a given crystal. Most estimates of shock duration in Martian meteorites (Walton et al. 2014 and references therein), are in the range of 1-

10ms, which would imply effective growth temperatures in the type example of 1470-1620K for 2.5 nm crystals of ringwoodite at ~23 μm from the shock melt pocket and 1860-2100K for a 500 nm ahrensite crystals at 1 μm from the shock melt. From Fig. 13, the very long shock duration of ~1s posited by Baziotis et al. (2013) to produce 2 μm ringwoodite crystals doesn't appear to be required, provided the effective temperature was high enough.

The discussion above tacitly assumes that the mechanism for grain growth of the type ahrensite was the same as that in Liu et al.'s (1998) experiments (solid lines in Fig. 13). We also show results for semi-coherent platelet growth in the [100] direction for a 1s shock based on experiments of Kerschhofer et al. (2000; dashed line in Fig. 13). We noted above that the growth mechanism for ahrensite is incoherent (i.e., not semi-coherent) but use the Kerschhofer et al. (2000) data to make the point that mechanism can have a large effect on the rate of grain growth, so that quantitative calculations based on experimental data require a match in mechanism. Were Kerschhofer et al.'s (2000) mechanism operative, very large shocks or very high temperatures would be required to account for the observed ahrensite-ringwoodite crystals. One can also imagine that growth rates might have been even faster in Tissint than in Liu et al.'s (1998) experiments, perhaps because the defect density in highly shocked olivine was much higher than in the experiments. Water may also have been influential. For example, Du Frane et al. (2013) showed that water contents of 75 - 300 ppm in precursor olivine enhanced the growth rate of ringwoodite; 100-300 ppm water content is not implausible for the Tissint olivines prior to impact (Boctor et al., 2009). This amount of water would also reduce the temperature of the olivine away from the melt pocket but not nearly enough to bring the temperature at 23 μm into alignment with the principal Hugoniot.

Overall, our analysis of Fig. 13 suggests that a relatively small (1-10 ms) shock can account for observed ahrensite grain sizes adjacent to the melt pocket. However, inferred effective temperatures 23 μm from the melt pocket are much higher than the principal Hugoniot of the "bedrock" at 20-30 GPa (Raikes and Ahrens, 1979; Ahrens et al., 1969). This implies that either (a) the heat transfer mechanism for shocked olivines in contact with melt pockets is not understood (e.g., conduction would not be fast enough) or (b) the mechanism(s) controlling growth of ringwoodite in strained olivine under dynamic compression have a much weaker dependence of growth rate on inverse temperature that those prevailing under static conditions.

5. SUMMARY

We present the first comprehensive set of crystallographic, quantitative chemical, and spectroscopic parameters of the new mineral ahrensite. We also report occurrence and grain size statistics of ringwoodite and ahrensite in olivine grains of the Tissint martian meteorite. Ringwoodite and ahrensite are common transformation products of shock-compressed olivine during the Tissint impact event. However, only in the vicinity of melt pockets is the transformation complete. We report, for the first time, the existence of a population of nano-crystalline ringwoodite in strained olivine at distances as much as 80 μm away from melt pockets observed in the plane of the section. We also give the first grain size statistics of ringwoodite and ahrensite as function of distance to the melt pocket (reflecting a temperature gradient) in both 2 and 3-D. The absence of any orientational relationship between olivine and ringwoodite or ahrensite indicates random nucleation and incoherent growth of these phases; grain growth in the dynamically stressed olivines of Tissint may be controlled by different mechanisms than growth under static conditions and this may account for why inferred temperatures at 20 μm or more from a melt pocket are so much greater than the background temperature expected from the principal Hugoniot. Grain sizes observed near interfaces with melt pockets are, however, consistent to first order with modest shock durations of 1-10 ms, assuming the experimentally determined rates for incoherent grain growth under static conditions to be pertinent.

ACKNOWLEDGEMENTS

SEM, EBSD and EPMA analyses were carried out at the Caltech GPS Division Analytical Facility, which is supported, in part, by NSF Grants EAR-0318518 and DMR-0080065. Synchrotron micro-diffraction was carried out at the 16-IDB beamline of the Advanced Photon Source. Use of the Advanced Photon Source, an Office of Science User Facility operated for the U.S. Department of Energy (DOE) Office of Science by Argonne National Laboratory, was supported by the U.S. DOE under Contract No. DE-AC02-06CH11357. OT was sponsored in part by the National Nuclear Security Administration under the Stewardship Science Academic Alliances program through DOE Cooperative Agreement #DE-NA0001982. LAT and JRB acknowledge the support from NASA Cosmochemistry grants NNX11AG58G and NNX12AH63G, respectively. GRR acknowledges the support from NSF grant EAR-1322082. YL acknowledges the support of JPL, which is managed by California Institute of Technology

under a contract with NASA. We thank Tom Sharp, Makoto Kimura and an anonymous reviewer for their constructive reviews.

REFERENCES

Ahrens T.J., Petersen C.F. and Rosenber J.T. (1969) Shock compression of feldspars. J. Geophys. Res. **74**, 2727–2746.

Akram M. and M. Anis-ur-Rehman (2013) Dependence of site occupancy and structural and electrical properties on successive replacement of Co by Zn in $CoFe_2O_4$. *J. Electronic Materials* **43**, 485–492.

Aoudjehane H.C., Avice G., Barrat J.-A., Boudouma O., Chen G., Duke M.J.M., Franchi I.A., Gattacceca J., Grady M.M., Greenwood R.C., Herd C.D.K., Hewins R., Jambon A., Marty B., Rochette P., Smith C.L., Sautter V., Verchovsky A., Weber P. and Zanda B. (2012) Tissint Martian meteorite: A fresh look at the interior, surface, and atmosphere of Mars. *Science* **338**, 785–788.

Armann M. and Tackley P.J. (2012) Simulating the thermochemical magmatic and tectonic evolution of Venus's mantle and lithosphere: Two-dimensional models. *J. Geophys. Res.* **117**, E12003, doi:10.1029/2012JE004231.

Armstrong J.T. (1995) CITZAF: a package of correction programs for the quantitative electron microbeam X-ray analysis of thick polished materials, thin films, and particles. *Microbeam Analysis* **4**, 177–200.

Baziotis I.P., Liu Y., DeCarli P.S., Melosh H.J., McSween H.Y., Bodnar R.J. and Taylor L.A. (2013) The Tissint Martian meteorite as evidence for the largest impact excavation. *Nature Comm.* 4, 1404. DOI: 10.1038/ncomms2414.

Bertka C.M. and Fei Y. (1997) Mineralogy of the Martian interior up to core-mantle boundary pressures. *J. Geophys. Res.* **102**, 5251–5264.

Binns R.A., Davis R.J. and Reed S.J.B. (1969) Ringwoodite, natural $(Mg,Fe)_2SiO_4$ spinel in the Tenham meteorite. *Nature* **221**, 943–944.

Bloch E. and Ganguly J. (2014) ^{176}Lu–^{176}Hf and ^{147}Sm-^{143}Nd ages of the Martian shergottites: Evaluation of the shock-resetting hypothesis through diffusion kinetic experiments and modeling, and petrological observations. *Earth Planet. Sci. Lett.* **395**, 173–183.

Boctor N.Z., Wang J., Alexander C.M.O'D., Steele A. and Armstrong J. (2009) Hydrogen isotope signatures and water abundances in nominally anhydrous minerals from the olivine-phyric shergottite LAR 06319. *Meteorit. Planet. Sci.* **44**, A35.

Bouvier A., Blichert-Toft J., Vervoort J.D., Gillet P. and Albarède F. (2008) The case for old basaltic shergottites. *Earth Planet. Sci. Lett.* **266**, 105–124.

Canup R.M. (2012) Forming a Moon with an Earth-like composition via a giant impact. *Science* **338**, 1052–1055.

Du Frane W.L., Sharp T.G., Mosenfelder J.L. and Leinenweber K. (2013) Ringwoodite growth rates from olivine with ~75 ppmw H_2O: Metastable olivine must be nearly anhydrous to exist in the mantle transition zone. *Phys. Earth Planet. Int*. **219**, 1–10.

El Goresy A., Gillet Ph., Miyahara M., Ohtani E., Ozawa S., Beck P. and Montagnac G. (2013a) Shock-induced deformation of shergottites: shock-pressures and perturbations of magmatic ages on Mars. *Geochim. Cosmochim. Acta* **101**, 233–262.

El Goresy A., Gillet Ph., Miyahara M., Ohtani E., Ozawa S., Lin Y., Feng L. and Escerig S. (2013b) Multiple shock events and diamond formation on Mars. *Lunar Planet. Sci. Conf*. **44**. 1037. pdf

Fassett C.I. and Minton D.A. (2013) Impact bombardment of the terrestrial planets and the early history of the solar system. *Nature Geosci*. **6**, 520–524.

Feng L., Lin Y., Hu S., Xu L. and Miao B. (2011) Estimating compositions of ringwoodite in the heavily shocked Grove Mountains 052049 meteorite from Raman spectra. *Am. Mineral*. **96**, 1480–1489.

Fritz J. and Greshake A. (2009) High-pressure phases in an ultramafic rock from Mars. *Earth Planet. Sci. Lett*. **288**, 619–623.

Fritz J., Artemieva N. and Greshake A. (2005) Ejection of Martian meteorites. *Meteoritics & Planet. Sci.* **40**, 1393-1411.

Greshake A., Fritz J., Böttger U. and Goran D. (2013) Shear-induced ringwoodite formation in the Martian shergottite Dar al Gani 670. *Earth Planet. Sci. Lett*. **375**, 383–394.

Hammersley A.P., Svensson S.O., Hanfland M., Fitch A.N. and Hausermann D. (1996) Two-dimensional detector software: From real detector to idealised image or two-theta scan. *High Press. Res.* **14**, 235–248.

Humayun M., Nemchin A., Zanda B., Hewins R.H., Grange M., Kennedy A., Lorand J.-P., Göpel C., Fieni C., Pont S. and Deldicque D. (2013) Origin and age of the earliest Martian crust from meteorite NWA 7533. *Nature* **503**, 513–516.

Irving A.J., Kuehner S.M., Tanaka R., Herd C.D.K., Chen G. and Lapen T.J. (2012) The Tissint depleted permafic olivine-phyric shergottite: petrologic, elemental and isotopic characterization of a recent Martian fall in Morocco. *Lunar Planet. Sci. Conf.* **43**. 2510. pdf

Keppler H. and Smyth J.R. (2005) Optical and near infrared spectra of ringwoodite to 21.5 GPa: Implications for radiative heat transport in the mantle. *Am. Mineral*. **90**, 1209–1212.

Kerschhofer L., Rubie D.C., Sharp T.G., McConnell J.D.C. and Dupas-Bruzek C. (2000) Kinetics of intracrystalline olivine-ringwoodite transformation. *Phys. Earth Planet. Inter.* **121**, 59–76.

Kimura M., Chen M., Yoshida T., El Goresy A. and Ohtani E. (2003) Back-transformation of high-pressure phases in a shock melt vein of an H-chondrite during atmospheric passage: Implications for the survival of high-pressure phases after decompression. *Earth Planet. Sci. Lett*. **217**, 141–150.

Kraus W. and Nolze G. (1996) POWDER CELL – a program for the representation and manipulation of crystal structures and calculation of the resulting X-ray powder patterns. *J. Appl. Crystall*. **29**, 301–303.

Liu M., Kerschhofer L., Mosenfelder J.L. and Rubie D.C. (1998) The effect of strain energy on growth rates during the olivine-spinel transformation. *J. Geophys. Res.* **103**, 23897-23909.

Luo S.-N., Germann T.C., Tonks D.L. and An Q. (2010) Shock wave loading and spallation of copper bicrystals with asymmetric Σ3<110> tilt grain boundaries. *J. Appl. Phys.* **108**, 093526.

Ma C. and Rossman G.R. (2008) Barioperovskite, $BaTiO_3$, a new mineral from the Benitoite Mine, California. *Am. Mineral*. **93**, 154–157.

Ma C. and Rossman G.R. (2009) Tistarite, Ti_2O_3, a new refractory mineral from the Allende meteorite. *Am. Mineral*. **94**, 841–844.

Ma C., Tschauner O., Liu Y. and Sinogeikin S. (2013) Ahrensite. IMA 2013-028. CNMNC Newsletter No. 16, August 2013, page 2707. *Mineral. Mag*. **77**, 2695–2709.

Ma C., Tschauner O., Liu Y., Beckett J.R., Rossman G.R., Zuravlev K., Prakapenka V., Dera P., Sinogeikin S., Smith J. and Taylor L.A. (2014a) Discovery of ahrensite γ-Fe_2SiO_4 and

tissintite (Ca,Na,□)$AlSi_2O_6$: two new high pressure minerals from the Tissint Martian meteorite. *Lunar Planet. Sci. Conf.* **45**. 1222. pdf

Ma C., Tschauner O., Beckett J.R., Yang L., Rossman G.R., Zuravlev K., Prakapenka V., Dera P., Sinogeikin S., Smith J. and Taylor L.A. (2014b) First new minerals from Mars: Discovery of ahrensite γ-Fe_2SiO_4 and tissintite (Ca,Na,□)$AlSi_2O_6$, two high pressure phases from the Tissint martian meteorite. *8th Intl. Conf. Mars*. 1317. pdf

Ma C., Tschauner O., Beckett J.R., Liu Y., Rossman G.R., Zhuravlev K., Prakapenka V., Dera P. and Taylor L.A. (2015) Tissintite, (Ca,Na,□)$AlSiO_6$, a highly-defective, shock-induced, high-pressure clinopyroxene in the Tissint martian meteorite. *Earth Planet. Sci. Lett.* **422**, 194-205.

Marchi S., Chapman C.R., Fassett C.L., Head J.W., Bottke W.F. and Strom R.G. (2013) Global resurfacing of Mercury 4.0-4.1 billion years ago by heavy bombardment and volcanism. *Nature* **499**, 59–61.

Mills S.J., Hatert F., Nickel E.H. and Ferraris G. (2009) The standardization of mineral group hierarchies: application to recent nomenclature proposals. *Eur. J. Mineral.* **21**, 1073–1080.

Miyahara M., Ohtani E., Kimura M., El Goresy A., Ozawa S., Nagase T., Nishijima M. and Hiraga K. (2010) Coherent and subsequent incoherent ringwoodite growth in olivine of shocked L6 chondrites. *Earth Planet. Sci. Lett.* **295**, 321–327.

Morbidelli A., Marchi S., Bottke W.F. and Kring D.A. (2012) A sawtooth-like timeline for the first billion years of lunar bombardment. *Earth Planet. Sci.* **355-356**, 144–151.

Mosenfelder J.L., Marton F.C., Ross C.R., Kerschhofer L. and Rubie, D.C. (2001) Experimental constraints on the depth of olivine metastability in subducting lithosphere. *Phys. Earth Planet. Int.* **127**, 165–180.

Murty S.V.S., Mahajan R.R., Kumar P.M.R. and Aoudjehane H.C. (2012) Noble gases in the Martian meteorite Tissint. *Meteorit. Planet. Sci.* **48**, A287.

Neukum G., Ivanov B.A. and Hartmann W.K. (2001) Cratering records in the inner solar system in relation to the lunar reference system. *Chronol. Evol. Mars.* **96**, 55–86.

Ohtani E., Kimura Y., Kimura M., Takata T., Kondo T. and Kubo T. (2004) Formation of high-pressure minerals in shocked L6 chondrite Yamato 791384: constraints on shock conditions and parent body size. *Earth Planet. Sci. Lett.* **227**, 505–515.

Pham H.H., Arman B., Luo S.N. and Çağin T. (2011) Shock compression and spallation of palladium bicrystals with a Σ5 grain boundary. *J. Appl. Phys.* **109**, 086107.

Putz H., Schön J.C. and Jansen M. (1999) Combined method for ab initio structure solution from powder diffraction data. *J. Appl. Crystall.* **32**, 864–870.

Raikes S.A. and Ahrens T.J. (1979) Post-shock temperatures in minerals. *Geophys. J. Roy. Astr. Soc.* **58**, 717–747.

Ringwood A.E. (1958) The constitution of the mantle–II Further data on the olivine-spinel transition. *Geochim. Cosmochim. Acta* **15**, 18–29.

Ringwood A.E. (1962) Prediction and confirmation of olivine-spinel transition in Ni_2SiO_4. *Geochim. Cosmochim. Acta* **26**, 457–469.

Ringwood A.E. (1963) Olivine-spinel transformation in cobalt orthosilicate. *Nature* **198**, 79-80.

Ringwood A.E. and Major A. (1966) Synthesis of Mg_2SiO_4–Fe_2SiO_4 spinel solid solutions. *Earth Planet. Sci. Lett.* **1**, 241–245.

Sharp T.G. and De Carli P.S. (2006) Shock effects in meteorites. In: Lauretta, D.S., McSween, H.Y. (Eds.), Meteorites and the Early Solar System II. University of Arizona Press, Tucson, pp. 653–677.

Shaw C.S.J. and Walton E. (2013) Thermal modeling of shock melts in Martian meteorites: Implications for preserving atmospheric signatures and crystallization of high-pressure minerals from shock melts. *Meteorit. Planet. Sci.* **48**, 758–770.

Steele A., McCubbin F.M., Fries M., Kater L., Boctor N.Z., Fogel M.L., Conrad P.G., Glamoclija M., Spencer M., Morrow A.L., Hammond M.R., Zare R.N., Vicenzi E.P., Siljeström S., Bowden R., Herd C.D.K., Mysen B.O., Shirey S.B., Amundsen H.E.F., Treiman A.H., Bullock E.S. and Jull A.J.T. (2012) A reduced organic carbon component in Martian basalts. *Science* **337**, 212–215.

Stixrude L. and Lithgow-Bertelloni C. (2011) Thermodynamics of mantle minerals - II. Phase equilibria. *Geophys. J. Int.* **184**, 1180–1213.

Stöffler D., Keil K. and Scott E.R.D. (1991) Shock metamorphism of ordinary chondrites. *Geochim. Cosmochim. Acta* **55**, 3845–3867.

Stöffler D., Ostertage R., Jammes C., Pfannschimidt G., Gupta P.R.S., Simon S.B., Papike J.J. and Beauchamp R.H. (1986) Shock metamorphism and petrography of the Shergotty achondrite. *Geochim. Cosmochim. Acta* **50**, 889–903.

Rossman G.R. and Taran M.N. (2001) Spectroscopic standards for four- and five-fold coordinated Fe^{2+} in oxygen-based minerals. *Am. Mineral*. **86**, 896–903.

Taran M.N. and Rossman G.R. (2001) Optical spectroscopic study of tuhualite and a re-examination of the beryl, cordierite, and osumulite spectra. *Am. Mineral.* **86**, 973-980.

Tomioka N. and Fujino K. (1997) Natural (Mg,Fe)SiO_3-ilmenite and –perovskite in the Tenham meteorite. *Science* **277**, 1084–1086.

Tschauner O., Willis M.J., Asimow P.D. and Ahrens T.J. (2005) Effective liquid metal-silicate mixing upon shock by power-law droplet size scaling in Richtmyer-Meshkov like perturbations *Lunar Planet. Sci. Conf*. **36**, 1802. pdf

Tschauner O., Asimow P.D., Kostandova N., Ahrens T.J., Ma C., Sinogeikin S., Liu,Z., Fakra S. and Tamura N. (2009) Ultrafast growth of wadsleyite in shock-produced melts and its implications for early solar system impact processes. *Proc. Natl. Acad. Sci*. **106**, 13691–13695.

Tschauner O., Ma C., Beckett J.R., Prescher C., Prakapenka V. and Rossman G.R. (2014) Discovery of bridgmanite, the most abundant mineral in Earth, in a shocked meteorite. *Science* **346**, 1100–1102.

Walton E.L., Sharp T.G., Hu J. and Filiberto J. (2014) Heterogeneous mineral assemblages in martian meteorite Tissint as a result of a recent small impact event on Mars. *Geochim. Cosmochim. Acta* **140**, 334–348.

Xie Z. and Sharp T.G. (2007) Host rock solid-state transformation in a shock-induced melt vein of Tenham L6 chondrite. *Earth Planet. Sci. Lett*. **254**, 433–445.

Xie Z., Tomioka N. and Sharp T.G. (2002) Natural occurrence of Fe_2SiO_4-spinel in the shocked Umbarger L6 chondrite. *Am. Mineral*. **87**, 1257–1260.

Xie Z., Sharp T.G. and DeCarli P.S. (2006) High-pressure phases in a shock-induced melt vein in the Tenham L6 chondrite: Constraints on shock pressure and duration. *Geochim. Cosmochim. Acta* **70**, 504-515.

Zhang A.-C., Hsu W.-B., Floss C., Li X.-H., Li Q.-L., Liu Y. and Taylor L.A. (2011) Petrogenesis of lunar meteorite Northwest Africa 2977: Constraints from in situ microprobe results. *Meteorit. Planet. Sci*. **45**, 1929–1947.

Table 1

Electron microprobe analytical results for the melt pocket shown in Figs. 1-2 and associated phases including type ahrensite.

Constituent	ahrensite	ringwoodite	$(Mg,Fe)SiO_3$ + wüstite	olivine (core)	olivine (rim)	augite	pigeonite	plagioclase glass	melt pocket
	n=7[a]	n=4	n=6	n=3	n=3	n=2	n=3	n=7	n=5
SiO_2	34.9(0.1)[b]	36.0(0.3)	34.6(0.1)	36.3(0.3)	33.1(0.6)	52.4(0.5)	52.1(0.4)	54.5(0.4)	43.8(0.5)
TiO_2	b.d.[c]	b.d.	b.d.	b.d.	b.d.	0.29(0.03)	0.29(0.08)	b.d.	0.38(0.01)
Al_2O_3	b.d.	b.d.	b.d.	b.d.	b.d.	1.7(0.2)	1.1(0.3)	28.9(0.3)	4.1(0.6)
FeO	43.8(0.3)	39(1)	45.0(0.5)	31.3(0.4)	48(2)	13.8(0.1)	21(2)	1.08(0.06)	28.4(0.8)
MgO	21.1(0.2)	24.8(0.9)	19.7(0.3)	31.6(0.3)	18(1)	16.8(0.4)	17.6(0.9)	0.13(0.01)	14.6(0.5)
CaO	b.d.	b.d.	0.35(0.01)	b.d.	b.d.	13.9(0.5)	7(1)	11.9(0.1)	6.7(0.4)
Na_2O	b.d.	b.d.	b.d.	b.d.	b.d.	0.13(0.01)	0.08(0.02)	3.4(0.3)	0.6(0.1)
K_2O	b.d.	b.d.	b.d.	b.d.	b.d.	b.d.	b.d.	0.17(0.02)	0.02(0.01)
Cr_2O_3	b.d.	b.d.	b.d.	b.d.	b.d.	0.81(0.07)	0.5(0.1)	b.d.	0.18(0.04)
MnO	0.75(0.07)	0.67(0.04)	0.85(0.05)	0.60(0.03)	0.90(0.03)	0.45(0.03)	0.68(0.05)	b.d.	0.61(0.03)
Total	100.6	100	100.5	99.8	100	100.3	100.4	100.1	99.4
Mg/(Mg+Fe) atomic ratio as %	46	53	44	64	40	69	60	17	48

[a]n = number of analyses.
[b]Errors given inside parentheses are one standard deviation of the mean based on all of the analyses.
[c]b.d.= below detection limit: 0.02 wt% Ti, 0.03 wt% Al, 0.01 wt% Ca, 0.03 wt% Na, 0.02 wt% K, 0.03 wt% Cr, 0.04 wt% Mn.

Table 2
Atom coordinates and site occupancies of type ahrensite.

	x/a	*y/b*	*z/c*	Occupancy	B_{iso}
Fe 16d	5/8	5/8	5/8	0.56(+/-3)	0.55(4)
Mg 16d	5/8	5/8	5/8	0.43(+/-3)	0.55(4)
Si 16d	5/8	5/8	5/8	0.03(-3/+0)	0.55(4)
Si 8a	0	0	0	0.98(+3/-0)	0.23(1)
Fe 8a	0	0	0	0.03(-3/+0)	0.23(1)
O 32e	0.748(5)	0.748(5)	0.748(5)	1	0.24(1)

Table 3
Observed X-ray powder diffraction data for ahrensite ($I_{rel} > 1$).

h	*k*	*l*	*mul*[a]	*d* [Å]	$\|F^{b}_{calc}\|$	$\|F_{exp}\|$	*D*(|*F*|)	I_{rel}[c]
-3	-1	-1	24	2.461	530.7	491.7	39.0	100.0
-2	-2	-2	8	2.356	157.2	157.2	0.0	3.79
-4	0	0	6	2.041	896.1	874.0	22.1	49.6
-3	-3	-1	24	1.873	175.6	179.5	-3.9	7.3
-4	-2	-2	24	1.666	192.5	192.0	0.5	5.4
-5	-1	-1	24	1.571	367.7	379.2	-11.5	20.0
-3	-3	-3	8	1.571	423.2	433.2	10.0	8.6
-4	-4	0	12	1.443	971.9	1000	-28.1	57.0
-5	-3	-1	48	1.38	102.1	114.6	-12.5	3.24
-4	-4	-2	24	1.36	1.8	1.7	0.1	0.1
-6	-2	0	24	1.291	157.7	160	-2.3	2.2
-5	-3	-3	24	1.245	319.7	325.8	-9.1	9.8
-6	-2	-2	24	1.231	156.7	181.4	-24.7	3.3
-4	-4	-4	8	1.178	473.1	478.9	-5.8	7.1
-7	-1	-1	24	1.143	97.6	101.3	-3.7	1.1
-5	-5	-1	24	1.143	63.0	69.6	-6.6	0.5
-6	-4	-2	48	1.091	134.2	128.3	5.9	2.7
-7	-3	-1	48	1.063	278.8	272.4	6.4	13.2
-5	-5	-3	24	1.063	248.2	243.7	4.5	5.4
-8	0	0	6	1.02	628.1	599.1	29.0	8.4
-7	-3	-3	24	0.997	95.6	101.0	-5.4	1.0
-6	-4	-4	24	0.99	1.1	1.1	0.0	0.1
-8	-2	-2	24	0.962	112.6	113.2	-0.6	1.1
-6	-6	0	12	0.962	114.6	115.5	-0.9	0.6
-7	-5	-1	48	0.943	224.3	205.1	19.2	10.0
-5	-5	-5	8	0.943	199.5	183.1	16.4	1.3
-6	-6	-2	24	0.936	132.4	150.5	-18.1	2.1

[a]multiplicity.
[b]the structure factor.
[c]intensity relative to the most intense peak.

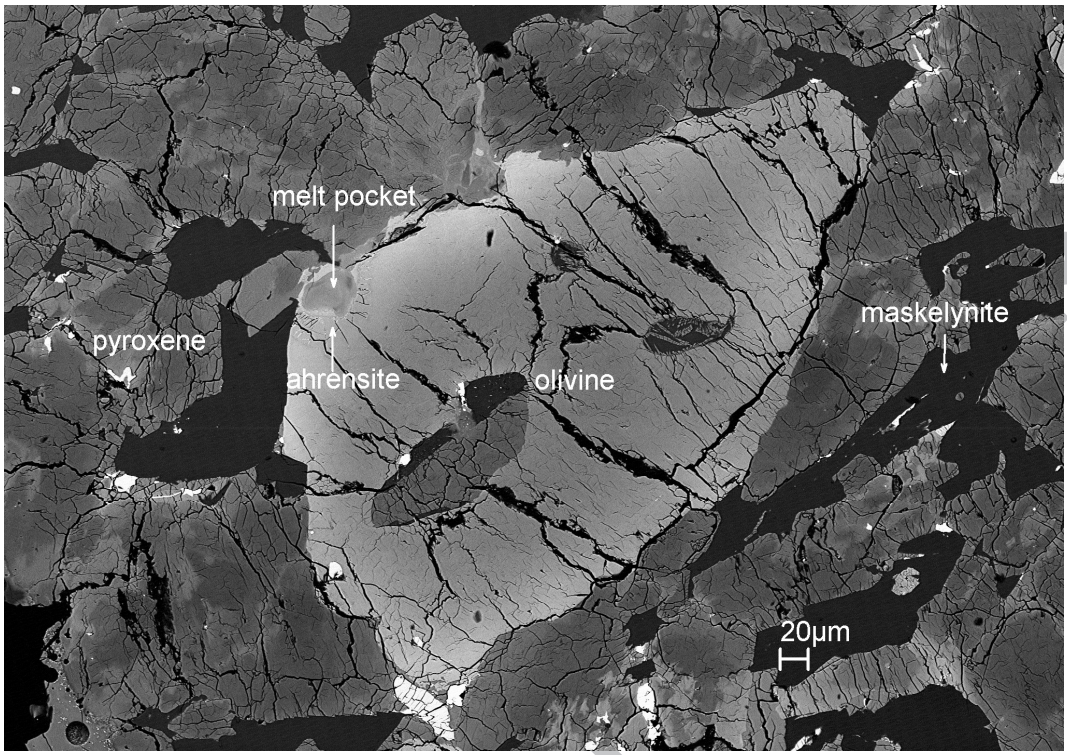

Fig. 1. Back-scatter electron (BSE) image of Tissint section UT2 showing overall texture and an olivine megacryst with type ahrensite and an associated shock melt pocket indicated.

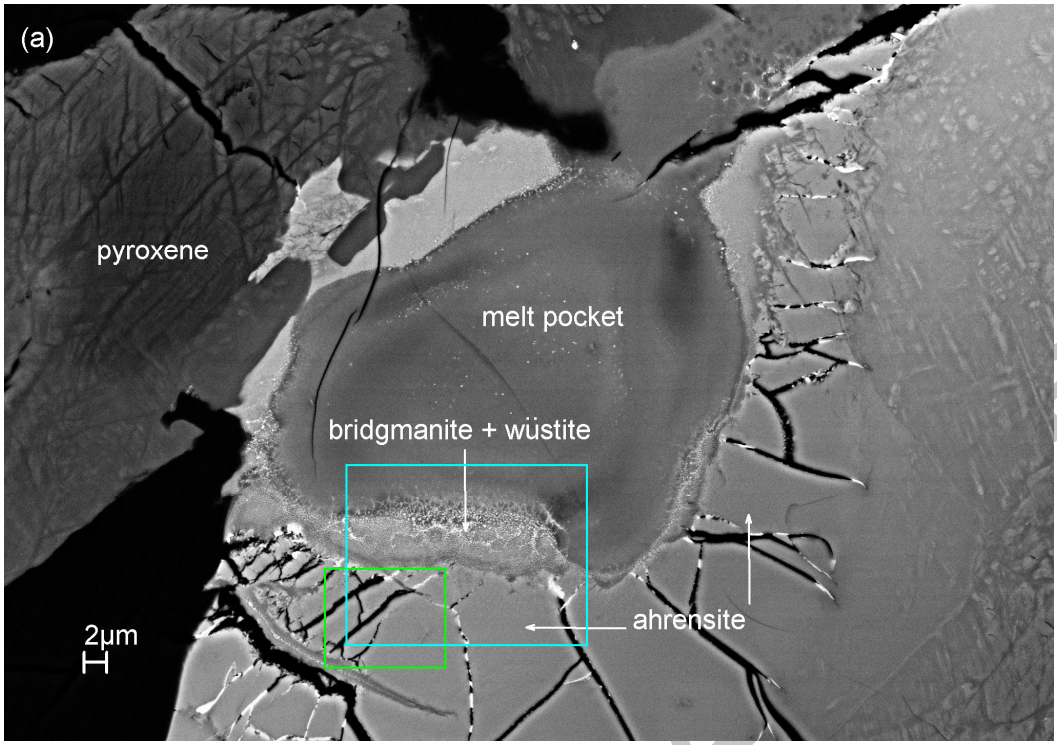
(a)
pyroxene
melt pocket
bridgmanite + wüstite
ahrensite
2μm

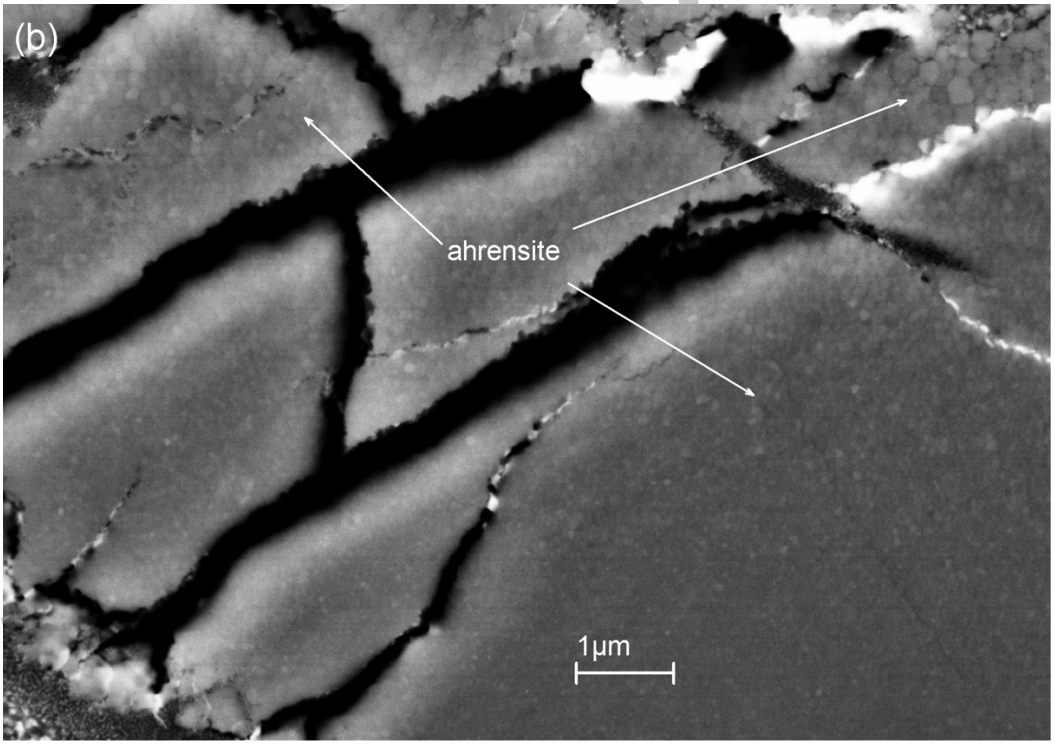
(b)
ahrensite
1μm

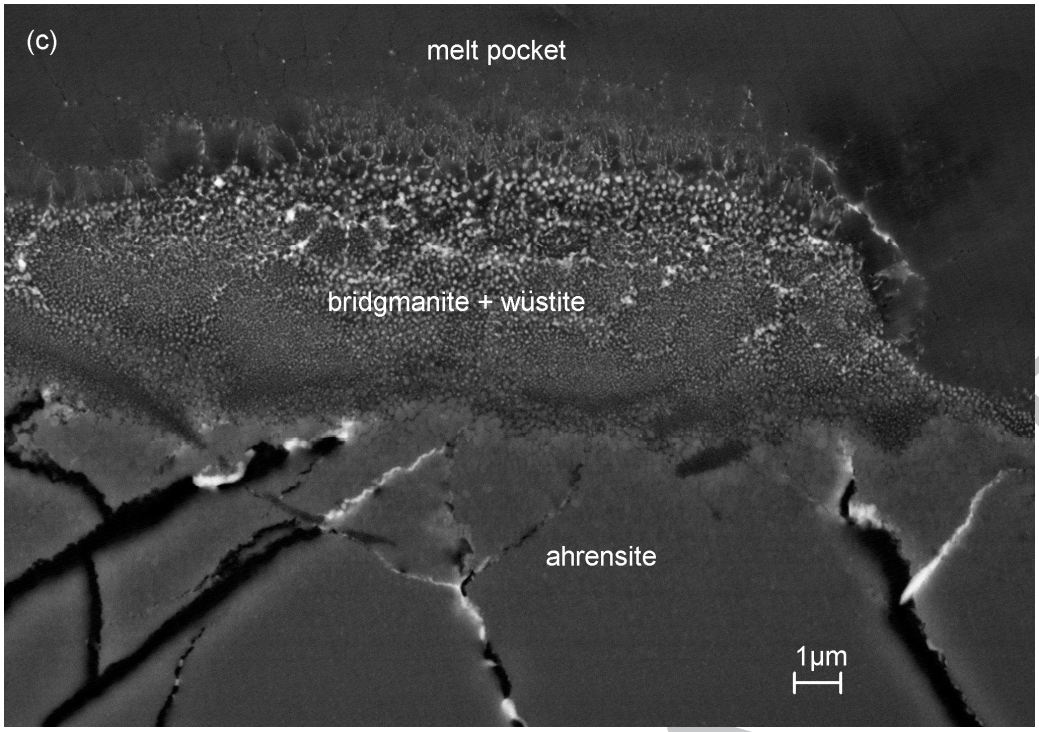

Fig. 2. Enlarged BSE images of the region near the melt pocket shown in Fig. 1b, revealing ahrensite domains and nearby phases. (a) An overview. The mottled area in the upper right shows no EBSD pattern and displays no Raman features. The white phase (in BSE) filling radial cracks extending across the ahrensite is FeS, likely a late vapor deposited phase. The two rectangles mark the areas of close-up images shown in panels b (green) and c (blue). (b) Close-up of submicrometer-sized to nanometer-sized polycrystalline ahrensite. (c) Close-up of "bridgmanite + wüstite" region in the panel.

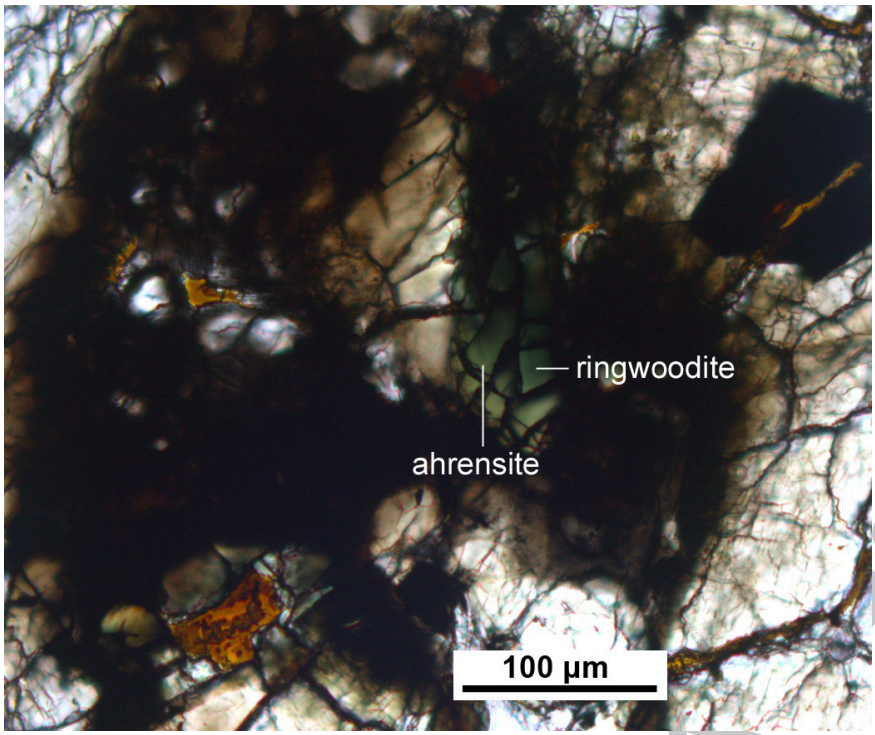

Fig. 3. Optical image under transmitted light showing ahrensite [$(Fe_{1.01}Mg_{0.95}Mn_{0.02})Si_{1.01}O_4$] - ringwoodite [$(Mg_{1.10}Fe_{0.86}Mn0_{.02})Si_{1.01}O_4$] with a bluish green color in UT1. The reddish-brown regions are openings filled with epoxy. Figure S2 gives a BSE image demonstrating the polycrystalline nature of ahrensite from a bluish-green area.

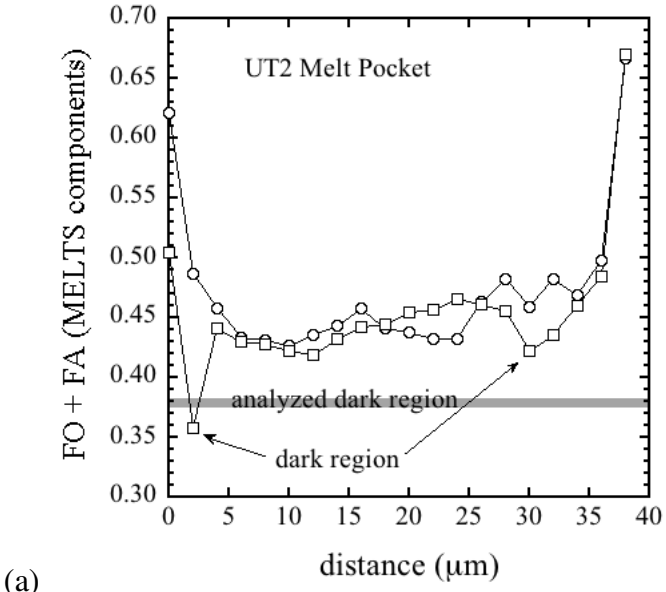

(a)

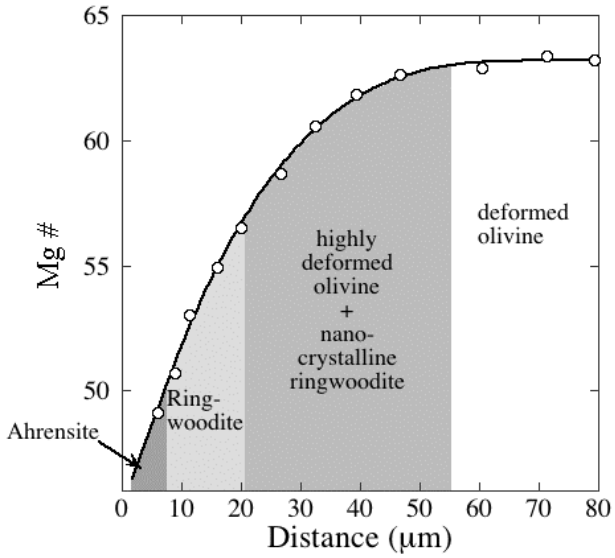

(b)

Fig. 4. Compositional variation of phases associated with type ahrensite. (a) Variation of the MELTS components Mg_2SiO_4 (FO) plus Fe_2SiO_4 (FA) across the melt pocket shown in Fig. 2a. Points labeled "dark region" sampled dark portions of the melt pocket. The average of 5 analyses in the largest dark region in the melt pocket of Fig. 2a is shown as a horizontal shaded bar. (b) Mg# as a function of distance along a traverse between melt pocket (bridgmanite plus wüstite occupies the region between 0 and 2 μm) and the interior of the olivine megacryst shown in Fig. 2. Between 2 and 21 μm, EBSD, Raman spectroscopy, and synchrotron diffraction all indicate crystalline ahrensite/ringwoodite. Between 21 and 55 μm, synchrotron diffraction indicates the presence of nanocrystalline ringwoodite but EBSD and Raman show no features. Beyond 55 μm, ringwoodite is not observed.

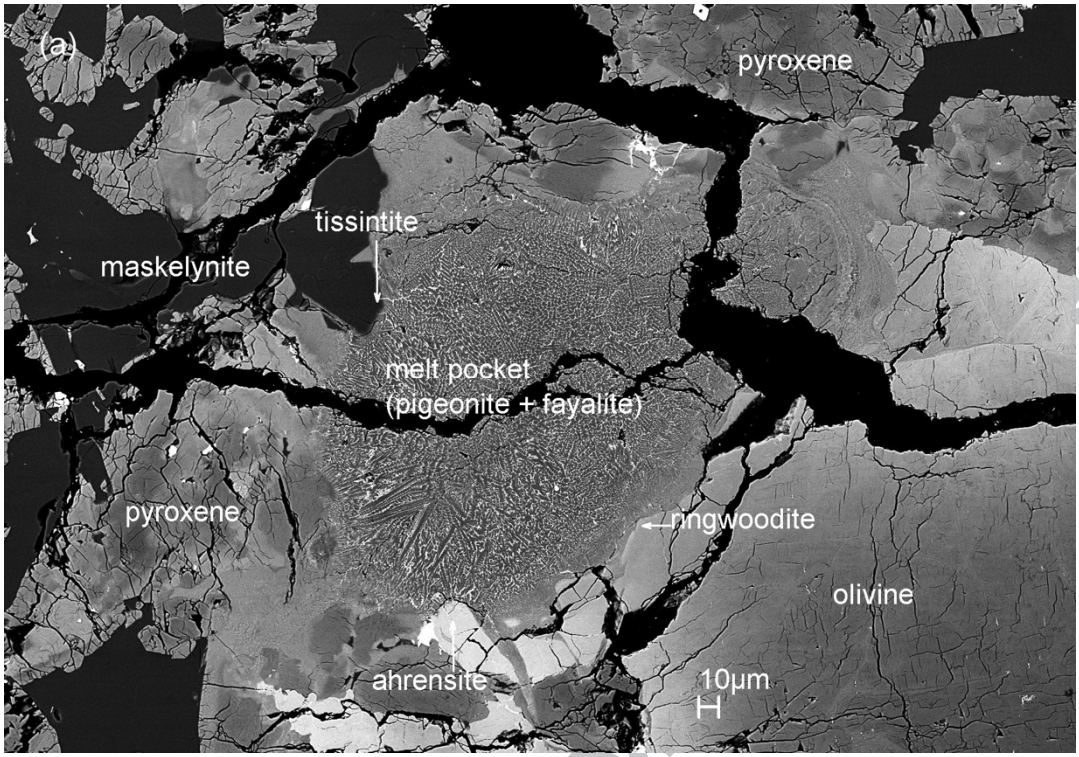

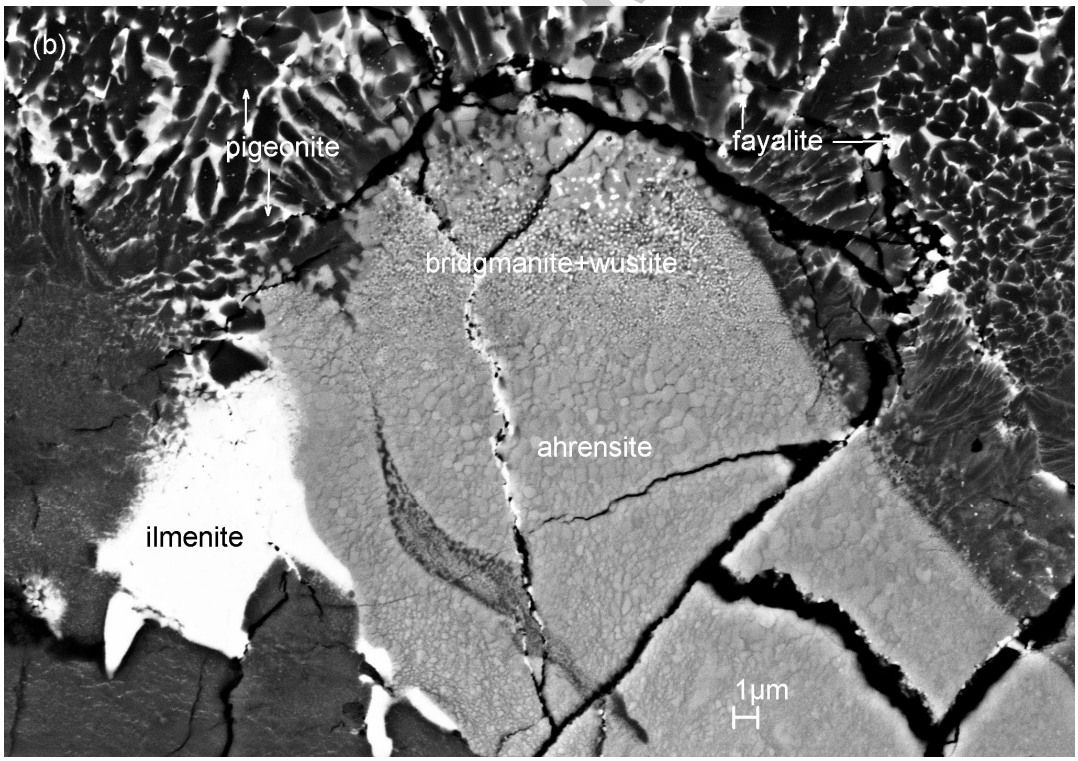

Fig. 5. BSE images of ahrensite and associated phases occurring adjacent to a large melt pocket region in Tissint section UT1. (a) overview. (b) close-up of a ringwoodite occurrence. See Fig. S3 for a close up of the ringwoodite labeled in panel a.

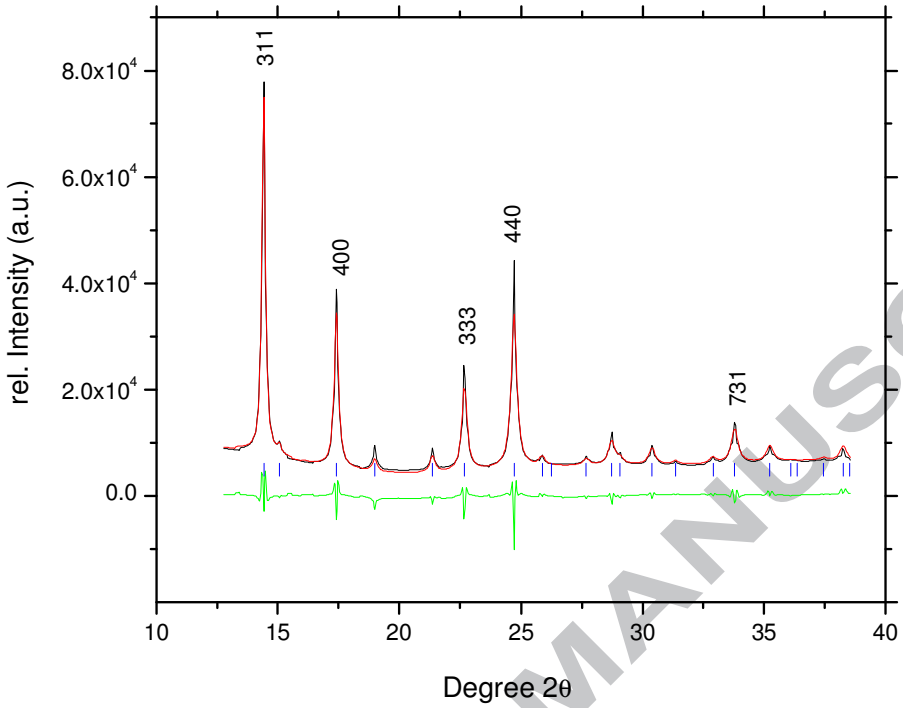

Fig. 6. Powder diffraction pattern of type ahrensite (black) with modeled diffraction pattern from Rietveld refinement (red), residual of fit (green) and positions of observed reflections indicated by blue tick marks. The wavelength of the primary X-ray beam was 0.6177 Å. The position of the spot was approximately 5 μm from the melt pocket shown in Fig. 2. Modeling of the (311) peak (the most intense peak in the figure; see text) yields an average grain size of 42 ± 3 nm.

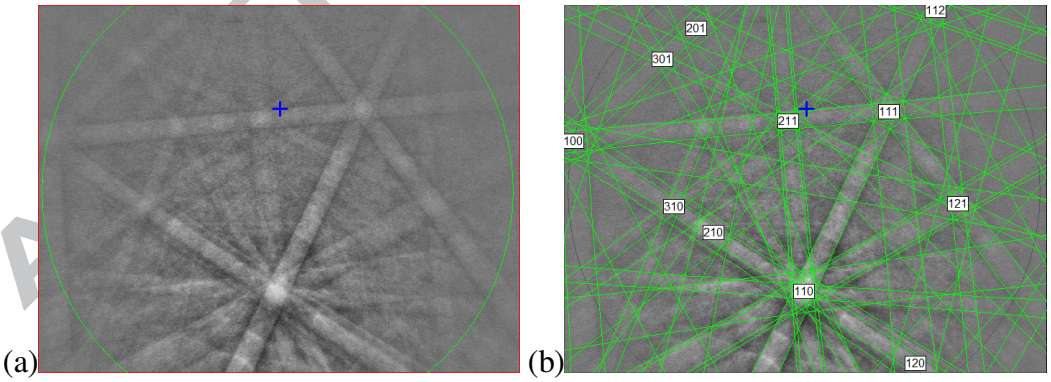

Fig. 7. (a) EBSD pattern of an ahrensite crystal in Tissint, (b) the pattern indexed using the ahrensite structure from synchrotron diffraction. In both panels, the blue cross indicates the center of the pattern.

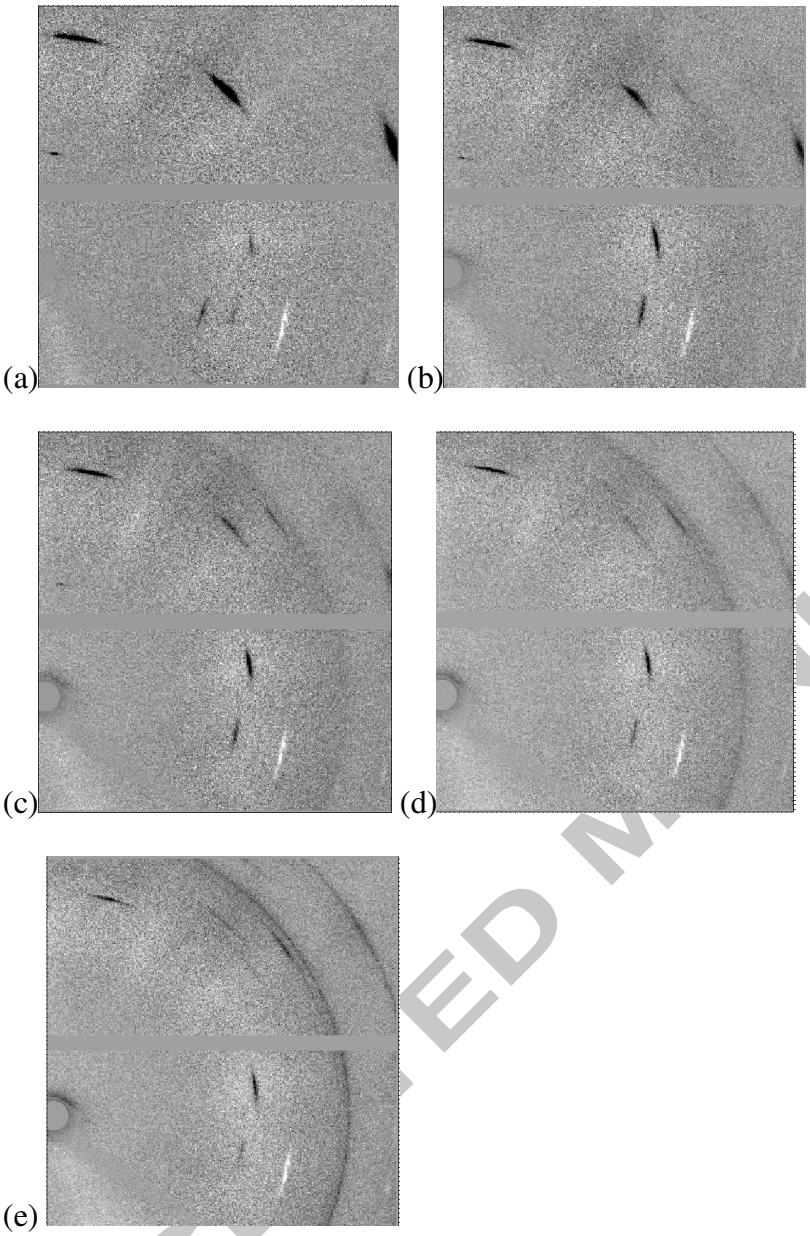

Fig. 8. Diffraction images of ringwoodite-ahrensite crystals growing in a strained olivine single crystal matrix as a function of distance from the shock-melt pocket in Fig. 1b. Elongated spots are olivine reflections. (a) 50 μm from melt pocket. The pattern exhibits no trace of silicate spinel. (b) 40 μm from melt pocket. Weak and very broad fringes of the 311 reflection of ringwoodite-ahrensite are present. The large peak width indicates nanocrystal grain sizes. (c) 30 μm from melt pocket. (d) 20 μm from melt pocket. (e) 10 μm from melt pocket. Note that panels (b – e) show the progressive growth of spinel-phase crystallites, both in amount and grain size (see also Fig. 9).

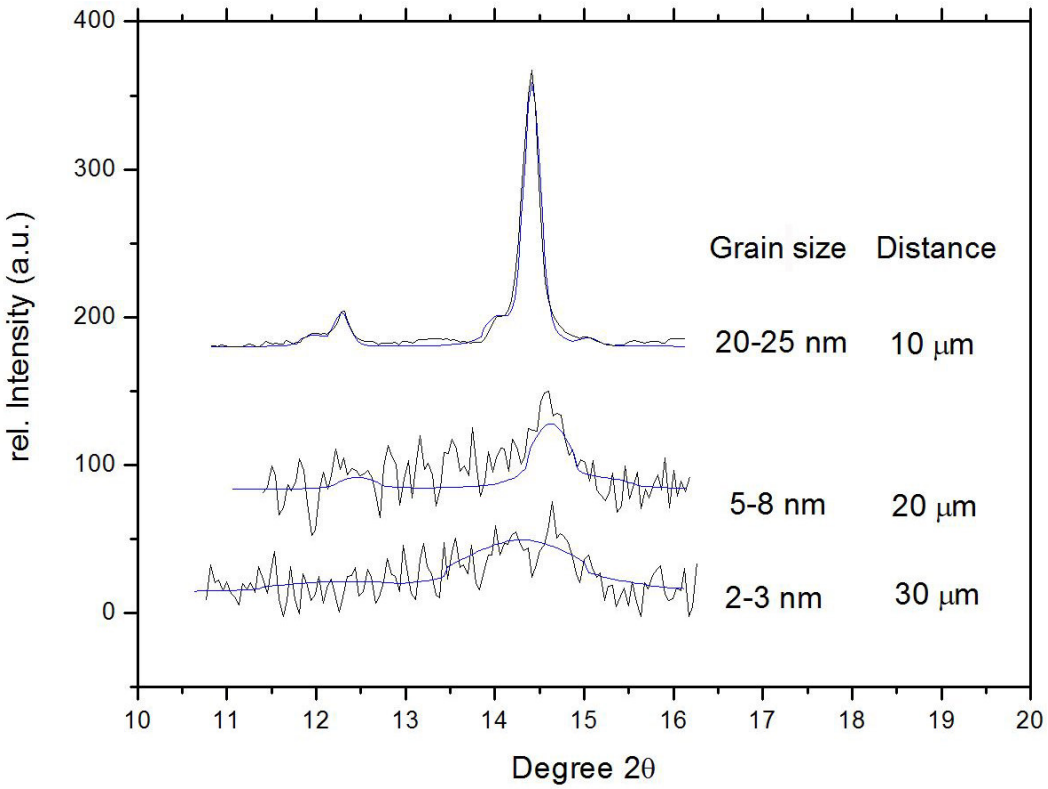

Fig. 9. Peak width and average grain size based on the (311) reflection for ahrensite-ringwoodite crystallites growing within a strained single crystal of olivine from Fig. 9c,d,e. The grain-size increases with decreasing distance from the melt pocket.

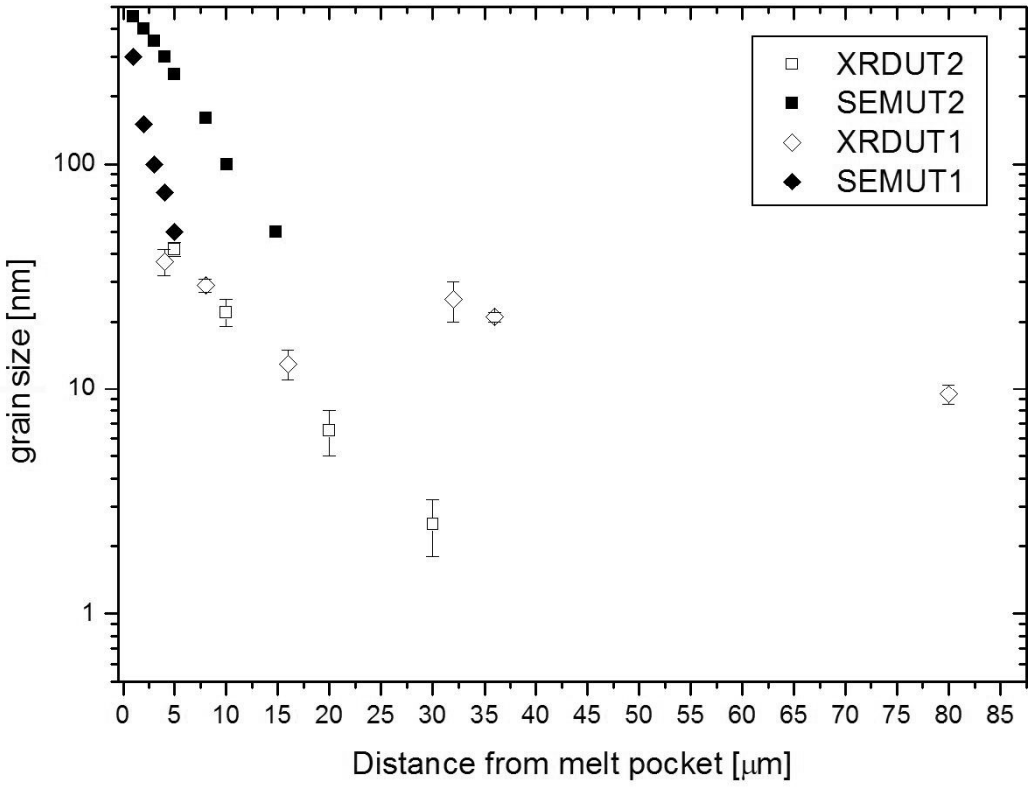

Fig. 10. Average grain size of ahrensite-ringwoodite crystals as a function of distance from the melt pocket. Data were obtained by either diffraction peak widths (XRDUT1 and XRDUT2) or visual measurements from BSE images (SEMUT1 and SEMUT2). Plotted errors bars in distance for synchrotron data reflect surface spot size (4×5 μm) but ignore possible differences in distance to the melt pocket as a function of depth (the beam passes through the entire sample). For the type region in section UT2 (Fig. 1b), the slopes for grain sizes derived from BSE and synchrotron XRD are similar (-0.05 vs. -0.07) but those from a UT1 olivine microphenocryst (40 × 60 μm) in contact with an elongate (50 × 330 μm) melt pocket differ by more than a factor of three.

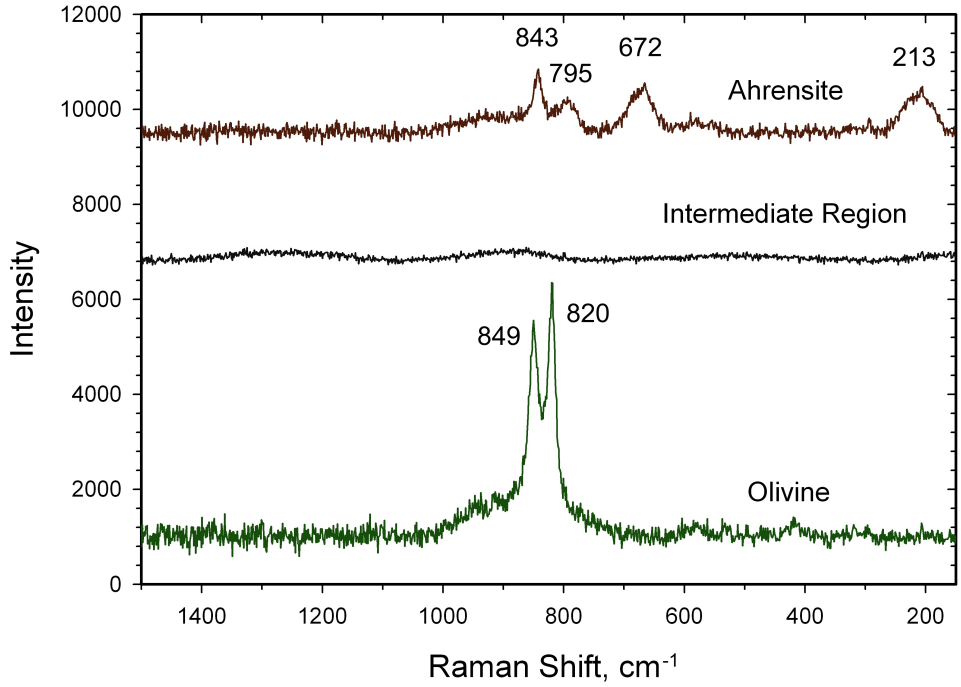

Fig. 11. Raman spectra of type ahrensite, olivine and the intermediate region between the two phases scaled to the same laser power and count time. Background is removed.

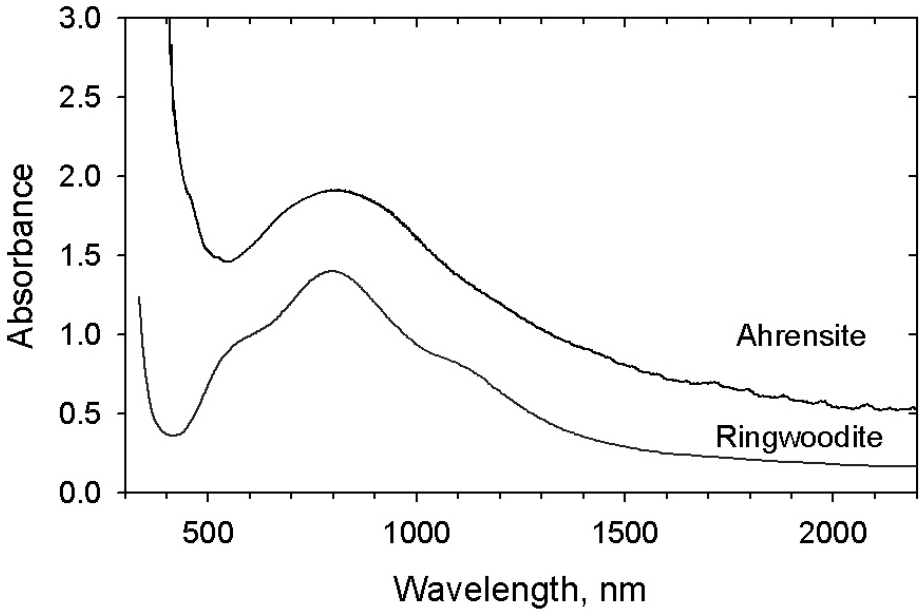

Fig. 12. Optical spectrum of ahrensite $(Fe_{1.01}Mg_{0.95}Mn_{0.02})Si_{1.01}O_4$ shown in Fig. 3 compared to the spectrum of ringwoodite $(Mg_{1.8}Fe_{0.2})SiO_4$ from Keppler and Smyth (2005).

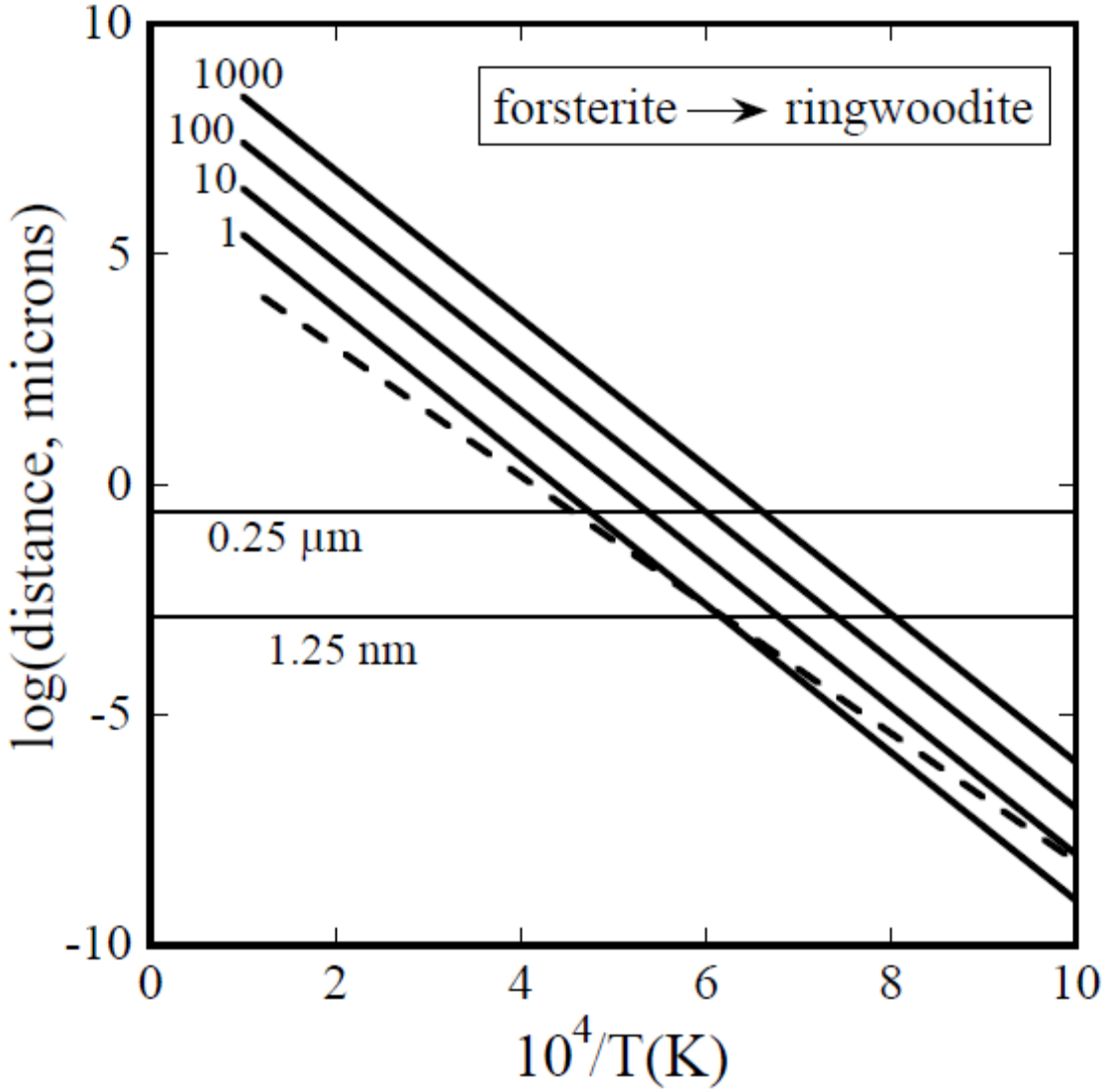

Fig. 13. Growth of ringwoodite from Mg_2SiO_4 forsterite after Kerschhofer et al. (2000) as a function of inverse temperature in degrees K. For incoherent growth [solid lines based on experiments of Liu et al. (1998)], results are presented for 1, 10, 100, and 1000 ms shocks. The dashed line refers to semi-coherent growth and a 1 s shock duration based on data of Kerschhofer et al. (2000). Horizontal lines are shown for 2.5 nm and 0.5 μm grains.